AGU PUBLICATIONS

JGR

Journal of Geophysical Research: Oceans

RESEARCH ARTICLE

10.1002/2017JC013078

The 2004 Sumatra Tsunami in the Southeastern Pacific Ocean: New Global Insight From Observations and Modeling

A. B. Rabinovich[1,2], V. V. Titov[3], C. W. Moore[3], and M. C. Eblé[3]

[1]Institute of Ocean Sciences, Sidney, BC, Canada, [2]P.P. Shirshov Institute of Oceanology, Moscow, Russia, [3]Pacific Marine Environmental Laboratory, NOAA, Seattle, WA, USA

Key Points:
- The 2004 Sumatra open-ocean and coastal tsunami measurements in the Southeastern Pacific are analyzed and modeled to study long-distance tsunami propagation
- Analysis of measurements and model time series revealed clear signatures of the tsunami source at locations over 18,000 km away
- Numerical model is able to reproduce key spectral and temporal tsunami characteristics of the tsunami after simulating over a day of propagation time

Correspondence to:
V. V. Titov,
vasily.titov@noaa.gov

Citation:
Rabinovich, A. B., Titov, V. V., Moore, C. W., & Eblé, M. C. (2017). The 2004 Sumatra Tsunami in the Southeastern Pacific Ocean: New global insight from observations and modeling. *Journal of Geophysical Research: Oceans*, *122*, 7992–8019. https://doi.org/10.1002/2017JC013078

Received 9 MAY 2017
Accepted 4 SEP 2017
Accepted article online 14 SEP 2017
Published online 24 OCT 2017

Abstract The 2004 Sumatra tsunami was an unprecedented global disaster measured throughout the world oceans. The present study focused on a region of the southeastern Pacific Ocean where the "westward" circumferentially propagating tsunami branch converged with the "eastward" branch, based on data from fortuitously placed Chilean DART 32401 and tide gauges along the coast of South America. By comparison of the tsunami and background spectra, we suppressed the influence of topography and reconstructed coastal "spectral ratios" that were in close agreement with a ratio at DART 32401 and spectral ratios in other oceans. Findings indicate that even remote tsunami records carry spectral source signatures ("birth-marks"). The 2004 tsunami waves were found to occupy the broad frequency band of 0.25–10 cph with the prominent ratio peak at period of 40 min related to the southern fast-slip source domain. This rupture "hot-spot" of ~350 km was responsible for the global impact of the 2004 tsunami. Data from DART 32401 provided validation of model results: the simulated maximum tsunami wave height of 2.25 cm was a conservative approximation to the measured height of 2.05 cm; the computed tsunami travel time of 25 h 35 min to DART 32401, although 20 min earlier than the actual travel time, provided a favorable result in comparison with 24 h 25 min estimated from classical kinematic theory. The numerical simulations consistently reproduced the wave height changes observed along the coast of South America, including local amplification of tsunami waves at the northern stations of Arica (72 cm) and Callao (67 cm).

1. Introduction

On 26 December 2004 at 00:59 UTC, a $M_w = 9.3$ megathrust earthquake occurred offshore of Sumatra, Indonesia rupturing 1,300 km of the oceanic subduction zone along the Sunda Trench in the East Indian Ocean (cf. Chlieh et al., 2007, Lay et al., 2005; Stein & Okal, 2005). The earthquake generated a global tsunami that severely impacted coastal regions of the Indian Ocean and stands as the world's deadliest in recorded history. Approximately 230,000 people in 14 countries around the Indian Ocean were killed; among the victims were citizens of more than 60 nations (Satake et al., 2007). The tsunami propagated throughout the world oceans and was recorded in remote regions of the North Pacific and North Atlantic, as far as 25–30,000 km from the source area (Titov et al., 2005; Rabinovich et al., 2006, Rabinovich, Candella, et al., 2011). The 2004 Sumatra (Indian Ocean) tsunami was a scientific watershed: tsunami research motivated by this event has progressed the scientific understanding of tsunami waves and was followed in the next decade by a dramatic change in tsunami detection, operational tsunami warning and forecast capabilities (Bernard & Titov, 2015, Kânoğlu et al., 2015; Rabinovich et al., 2015).

Tsunami waves generated by the 2004 event were recorded by numerous instruments sited in the Indian, Atlantic, and Pacific oceans (cf. Candella et al., 2008; Merrifield et al., 2005; Rabinovich & Thomson, 2007; Rabinovich et al., 2006, Rabinovich, Candella, et al., 2011; Thomson et al., 2007; Woodworth et al., 2005). The data from these instruments were widely used to examine essential properties of tsunami waves, including their propagation and transformation (Kowalik et al., 2007; Titov et al., 2005), reconstruction of the tsunami source (cf. Fine et al., 2005; Fujii & Satake, 2007), and estimation of tsunami energy decay (Rabinovich, Candella, et al., 2011). However, with a few notable exceptions, virtually all the 2004 tsunami records were from coastal tide gauges, where tsunami signals are typically strongly affected by local bathymetry and coastal topography, major resonant effects, wave refraction, and nonlinearity (Bernard et al., 2001; Mofjeld, 2009). As a consequence, identification of the fundamental tsunami properties, particularly with respect to the source characteristics, in these coastal records was intricate.

The only deep-ocean data in the Indian Ocean originally being used for comparison with numerical models were satellite altimetry measurements (Smith et al., 2005). The altimetry data were the primary input for most of tsunami source reconstruction modeling. Nevertheless, the satellite data had insufficient space resolution (along the rectilinear tracks), wave height accuracy limitations, and the high noise level, all of which contributed to uncertainties in defining the detailed tsunami source.

A very limited number of deep-ocean records of this event were available for analysis (cf. Rabinovich, Stroker, et al., 2011; Rabinovich, Woodworth, et al. 2011). The shortage of such data was especially unfortunate as these records provide more accurate characterization of tsunami waves, primarily due to a higher sampling rate coupled with a natural filtering of low-frequency related to the inverted barometer response to the air pressure oscillations and to steric effects, and high-frequency nonhydrostatic noise (Rabinovich & Eblé, 2015). Thus, open-ocean bottom pressure recorder (BPR) data are free of coastal effects and have very low background noise when compared with data recorded by coastal tide gauges (cf. Mofjeld, 2009). For these reasons, BPR records are valuable for investigating the physical aspects of the source region and specific properties of propagating tsunami waves. Open-ocean tsunami data also provide important constraints for tsunami model validation and specifying principal model source parameters (Rabinovich & Eblé, 2015; Titov, 2009). The advantage of BPR-based real-time tsunami monitoring and detection systems, such as the Deep-ocean Assessment and Reporting for Tsunamis (DART), led to priority in establishing a sensing array following the 2004 Sumatra tsunami and their incorporation as a key component of modern tsunami warning capabilities around the world (Bernard & Titov, 2015).

The DART system was specifically designed for open-ocean tsunami measurements and detection and, therefore, could have produced decisive data for the comprehensive examination of the 2004 Sumatra tsunami. Unfortunately, at the time of the 2004 event there were no DARTs operational in the Indian Ocean, while in the Pacific Ocean the entire experimental DART array included seven instruments and only two of them plus a similar NeMO BPR (e.g., Rabinovich, Stroker, et al., 2011) eventually provided high-quality 15 s data for this event: DART 46405 and NeMO in the northeastern part of the Pacific Ocean and DART 32401 in the southeastern part (Figure 1).

High-resolution (15 s) data recovered from the DART 32401 BPR was generously shared by system owner, Servicio Hidrográfico y Oceanográfico de la Armada de Chile (SHOA). This DART system was located offshore of the coast of northern Chile and was discovered to have fortuitously measured arrival of tsunami waves from the 2004 event quite clearly. This single DART system shows the value of each deep-ocean record in providing unique open-ocean *in situ* information on the far-field characteristics of tsunami waves. In the case of 2004 Sumatra, tsunami waves converged in this region from the Atlantic and Pacific oceans. Arrival at DART 32401 was approximately 26 h after the main shock, propagating a distance of approximately 18,000 km from the source (Figure 1). The 32401 BPR record provided the opportunity to investigate "pure" (undistorted by coastal effects) characteristics of the 2004 Sumatra tsunami waves and to compare them with the information gleaned from nearby coastal tide gauges along the mainland coast of South America and local islands. Together, these deep-ocean and coastal data provided validation of their scientific importance and the success of the global MOST numerical codes in resolving these complexities (Titov & González, 1997). The global MOST numerical model of the 2004 Sumatra tsunami, developed by Titov et al. (2005), enabled to describe the general character of the tsunami waves spreading in the world oceans, to specify some properties of these waves in particular regions and to overview the global impact of the 2004 Sumatra tsunami. Insufficient bathymetry available at that time, absence of open-ocean measurements and precise far-field coastal data, did not allow to validate the model and to get quantitative estimates of its efficiency and precluded direct comparison of modeled tsunami waveforms to those actually observed. As a result, comparison with recorded data was rather qualitative than quantitative. The data from remote DART 32401, located in 18,000 km from the source region, as well as from a number of tide gauges at the Pacific coast of South America, enable us to perform direct model-to-data comparisons and to assess the model accuracy quantitatively. The new data provided the basis upon which to test the MOST model performance at extra-long spatial and time scales and to examine the general behavior of generated tsunami waves in the southeastern Pacific.

Studies that include tsunami modeling over great distances, and compare with actual far-field observations, are a unique opportunity for global model validations. These studies allow estimating modeling accuracy limits and testing their application to the real-time tsunami forecast. The NOAA forecast system is based on

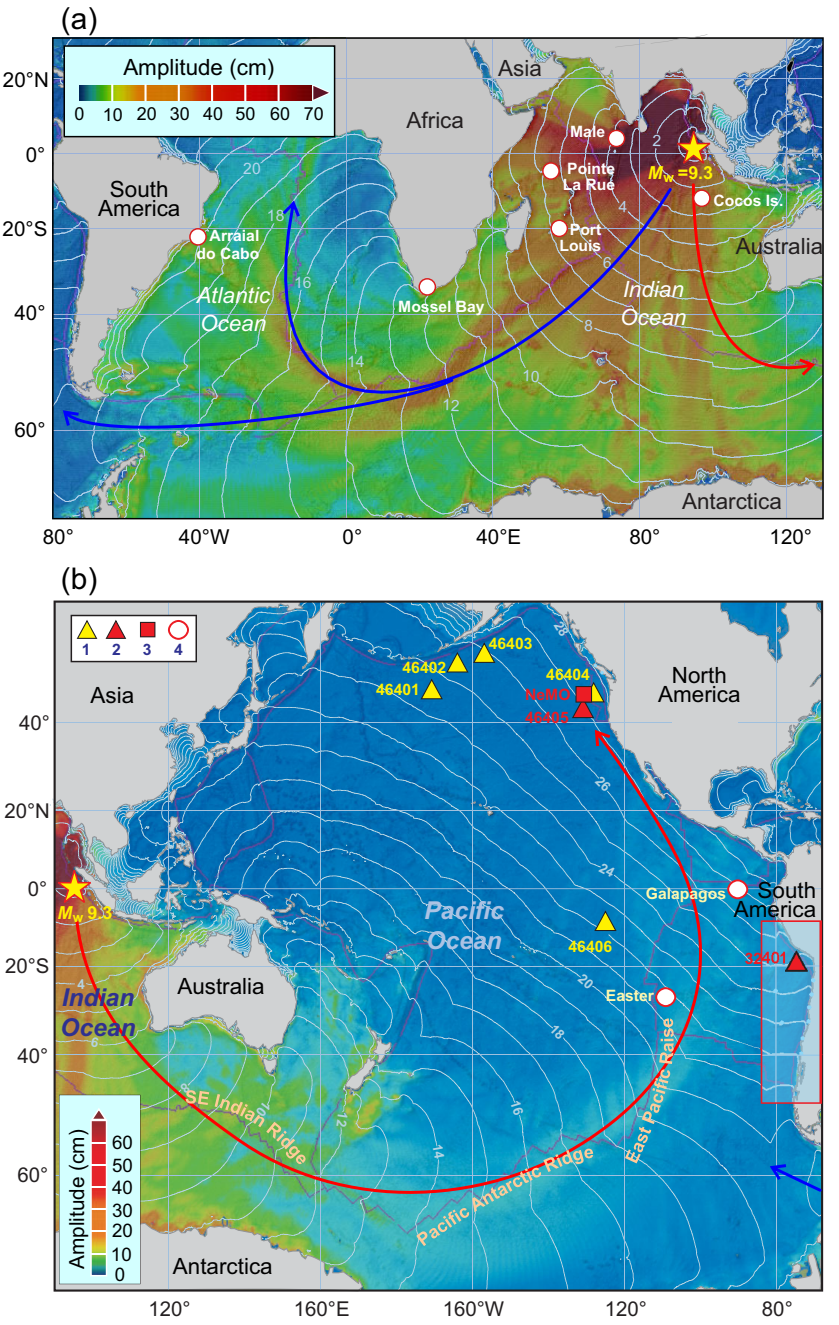

Figure 1. Locations of selected tide gauge stations (white circles) and DART systems operating in December 2004 superimposed on simulated 2004 maximum tsunami wave heights (from Titov et al. (2005)). The isochrones (solid white lines) show tsunami travel time (in hours) from the 2004 Sumatra earthquake source (epicenter marked by yellow star). The blue ("Atlantic" or "westward") and red ("Pacific" or "eastward") arrows show the computed tsunami energy flux propagating mainly along the mid-ocean ridges. (a) The tsunami energy flux spreading across the Indian Ocean into the Atlantic and Pacific oceans. (b) The energy flux propagating from the Indian Ocean into the Pacific Ocean: "1" are the stations that provided 15 min data; "2" are two DART stations (46405 and 32401) with available 15 s data; "3" is NeMO station in the northeastern Pacific; "4" are two island tide gauge stations, Galapagos (Baltra) and Easter Island, located beyond the main study region denoted by the red box.

the MOST numerical model (Titov & González, 1997; Titov & Synolakis, 1998; Titov, Kânoğlu, et al., 2016) for coastal inundation forecasts and results have been well vetted. In the present study, the MOST model was used for the high-resolution global modeling of the 2004 Sumatra tsunami to examine the wave field in the

southeastern Pacific Ocean and to estimate model uncertainties for the long-range tsunami forecast. While the presented numerical results are model-specific, the essential aspects of the simulation tend to be more general and may be important for overall problems of tsunami modeling.

The 2004 Sumatra tsunami was clearly recorded along the entire Pacific coast of South America with maximum wave heights measured at Arica, Northern Chile (72 cm) and at Callao, Peru (68 cm) (Rabinovich, Candella et al., 2011). In addition, high-quality tsunami records for this event were obtained at three Chilean island stations; Easter (Pascua) Island, Juan Fernandez Island, and San Felix Island, and at Galapagos Islands, Ecuador, where wave heights from 8 to 39 cm were measured. While the tsunami signal is clearly identified in all records, the signal-to-noise ratios were generally low, making it difficult to rely only on time domain comparison and analysis. To overpass this problem, we combined the frequency domain analysis with the time-domain comparisons to extract the tsunami arrival times and other tsunami characteristics from the time-series. The three types of tsunami records; open-ocean, island, and coastal mainland, when combined with the results of numerical modeling, provided a means to examine the basic properties of the observed waves and to compare them with those in the near-source area.

Two primary questions were addressed as the study progressed:

1. Were any particular spectral properties ("birth marks") of the 2004 tsunami records specifically related to this event and could they be identified with far-field records?
2. Could numerical tsunami models reproduce the tsunami characteristics (both spectral and temporal), thus validating model results and lending confidence in results during forecast and warning operations even on global scales?

It should be noted that despite hundreds of papers written on the 2004 Sumatra tsunami, very little attention has been paid to the Pacific coast of South America and the Southeast Pacific, in general. The respective tsunami records had not before been carefully examined, with the exception of Rabinovich, Candella, et al. (2011) who used these data to estimate tsunami energy decay. The study presented here focused on analysis of the 15 s BPR record offshore of Chile and on the coastal tide gauge records to determine the basic properties of the 2004 tsunami.

2. Tsunami Measurements

DART technology (as well as modern cable observatories, deployed offshore of Japan and Canada (e.g., Rabinovich & Eblé, 2015)) provides, arguably the most effective means to monitor, detect, and measure tsunami waves in the open-ocean. The technology is efficiently used both for tsunami research and for real-time operational tsunami warning (Bernard et al., 2001; González et al., 2005; Mofjeld, 2009). The system operates in two modes: (1) "standard operating mode" with four samples per hour transmitted via satellite at 6 h intervals; and (2) "event mode" during which data are transmitted in real time, a few minutes of full 15 s resolution and then a series of 1 min averages at predefined intervals. Although not returned in real-time, bottom pressure is internally recorded at the higher resolution 15 s intervals and are available for analysis after physical recovery of a bottom pressure recorder unit (Mungov et al., 2013).

Six US-owned DART systems were in operation in the Pacific Ocean during the December 2004 Sumatra earthquake and tsunami (Figure 1) (Rabinovich & Eblé, 2015). Unfortunately, tsunami amplitude at these stations were below the automatic "event mode" triggering threshold and the technology did not yet have two-way communication so these stations did not report "event mode" data in real-time. The high-resolution (15 s) data were later retrieved from the BPR internal storage after recovery in 2006, but only from one of the US stations; DART 46405, located in the Northeast Pacific (Figure 1). These data were analyzed and examined by Rabinovich, Stroker, et al. (2011) who identified in the record a very clear yet small amplitude tsunami signal.

Recently, one more deep-ocean record of this event became available at DART 32401, owned by Servicio Hidrografico y Oceanografico Armada de Chile (SHOA) (Rabinovich & Eblé, 2015). This DART system was deployed at a depth of 4517 m, approximately 480 km southwest of Arica, Chile at 19.548° S, 74.814° W (Figure 2). As was the case for DART 46405, internally recorded high-resolution (~0.5 mm) 15 s data were retrieved from the instrument after BPR recovery. The tsunami waves identified in the Chile DART 32401 record were better delineated and larger than those measured by DART 46405 in the northeastern Pacific

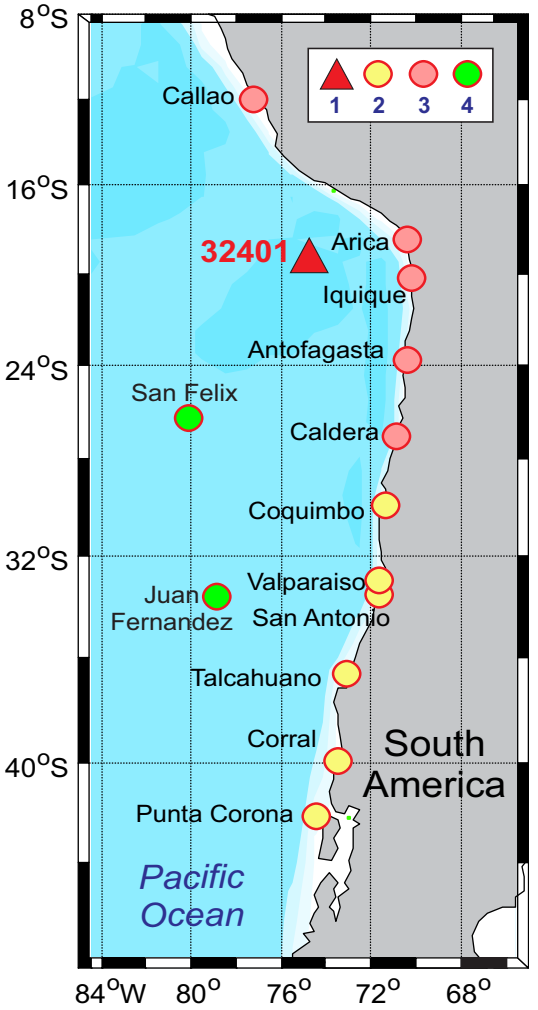

Figure 2. Map of the main study area, the Pacific coast of South America, on which is plotted the locations of (1) DART 32401 and coastal tide gauges from (2) "southern," (3) "northern" and (4) "island" groups of stations that were operational in December 2004. Station Galapagos (Baltra) from the "northern" group and Easter Island (Pascua) from the "island" group are shown in Figure 1.

(Rabinovich, Stroker, et al., 2011). As a result, these data proved invaluable for the 2004 tsunami investigation presented here.

DART data were supported by 15 coastal tide gauges: 13 from Chile, one from Peru, and one from Ecuador. Of these 15 stations, 11 were along the mainland South American coast (Figure 2) and 4 were coastal island stations on Juan Fernandez and San Felix (shown in Figure 2), and on Easter (Pascua) and Galapagos (the stations are indicated in Figure 1). The sampling interval of all coastal records was $\Delta t = 2$ min.

For open-ocean tsunami detection, a pressure recorder installed on the seafloor at several kilometres of water depth is generally required to measure and record sea level variations on order 0.1 cm amplitude. The challenge then becomes one of tsunami wave identification, i.e., distinguishing tsunami fluctuations from other processes that can have amplitudes 100–1,000 times greater than the tsunami. The process of tsunami isolation is generally based on the consecutive improvement of the signal-to-noise (s/n) ratio. The main principle of "*Do not distort a tsunami signal while extracting it*" was adhered to during the study's analyses phase discussed in the following section.

3. Tsunami Identification

The procedure followed for isolation of tsunami waves embedded in the time series records was the same as that described by Rabinovich et al. (2006), Rabinovich, Candella, et al. (2011), Rabinovich, Stroker, et al. (2011), and Rabinovich and Eblé (2015). Raw data as recorded were quality controlled before issues specific to individual time series records were addressed. Spikes and data shifts were prevalent in some records. Particular attention was paid to DART 32401 and coastal tide gauge time series to ensure that errors, spikes and shifts were correctly identified and then carefully remediated.

In general, the ability to identify tsunami waves and separate them from other signals in a sea level record strongly depends on the s/n ratio, i.e., on the ratio between tsunami wave height and site dependent background noise. Where the data are available, the s/n ratio for the 2004 Sumatra tsunami, ranged from 40:1 to 25:1 (Rabinovich & Thomson, 2007). The signal was high and essentially swamped background noise so extracting the tsunami was straightforward. However, at Pacific Ocean stations, the s/n ratio ranged from 6:1 to 1:1, or even lower for certain sites, making tsunami identification challenging.

Processing of coastal tide gauge and deep ocean BPR data (de-tiding, low-pass and high-pass filtering, etc.) was undertaken to diminish the noise level and thereby improve the s/n ratio without affecting the tsunami signal itself. Rabinovich, Stroker, et al. (2011) and Rabinovich and Eblé (2015) exemplified this process with extraction of the 2004 Sumatra tsunami from DART 46405 and NeMO (northeastern Pacific) records. The same approach was used here to isolate the 2004 tsunami at DART 32401. Figure 3a shows the initial time series from this DART. Visual identification of the tsunami is virtually impossible, as the local tide dominates the record, thus obscuring any trace of tsunami waveforms.

In the first step of tsunami isolation, astronomical tides were predicted by the least squares method of harmonic tidal analysis (cf. Foreman, 1977 [2004]; Pugh, 1987) and subsequently subtracted from the original series to yield a residual series. Altogether 13 tidal constituents were estimated; the dominant were the semidiurnal and diurnal harmonics M_2 (21.3 cm), K_1 (15.1 cm), O_1 (6.8 cm), S_2 (4.5 cm) and N_2 (3.4 cm). The original variance of the DART 32401 series was $\sigma^2_{orig} = 361.3$ cm^2, the variance of the computed tide was $\sigma^2_{tide} = 359.1$ cm^2 and the variance of the residual series was $\sigma^2_{res} = 2.2$ cm^2. This means that tides accounted for 99.39% of the total signal, leaving just 0.61% of the record partitioned between tsunami, background noise, atmospheric effects, and transient waves. It is important to emphasize here that subtraction of predicted tides from a time series does not distort or otherwise affect the tsunami signal. The standard de-tide

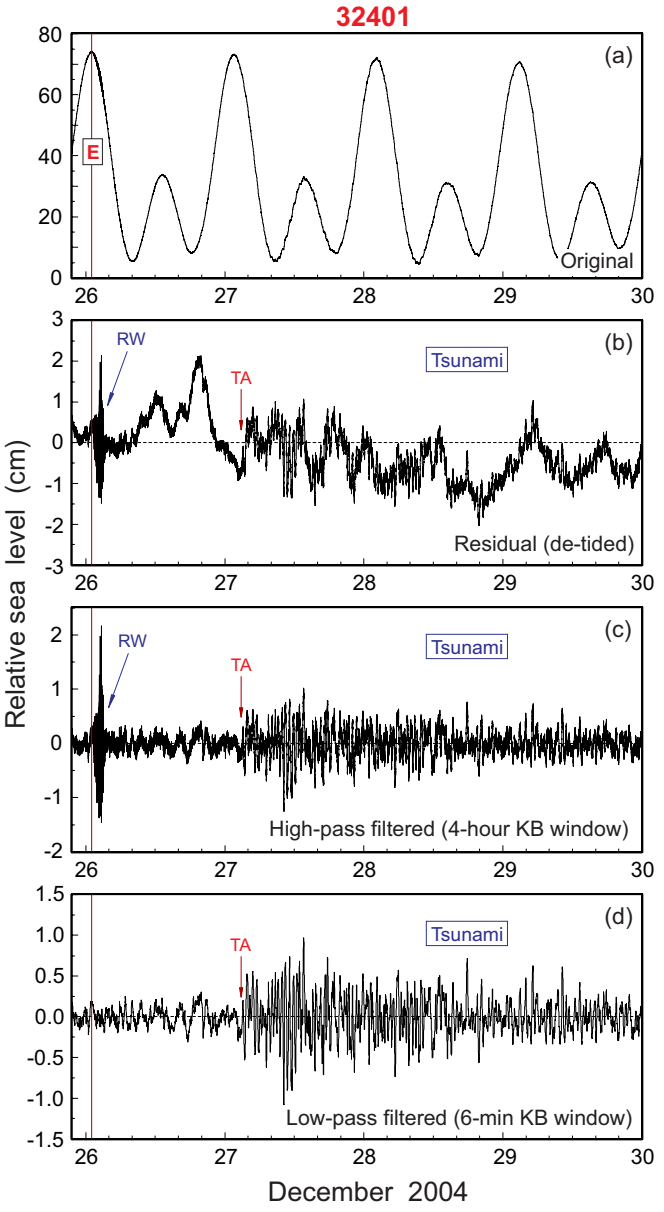

Figure 3. Graphical representation of the iterative analysis of the south-eastern Pacific DART 32401 record leading to exposure of the tsunami signal recorded during the 2004 Sumatra tsunami. (a) The original record shown strongly dominated by ocean tides. (b) The residual time series after subtraction of predicted tides from the original record. Low-frequency oscillations predominate. Seismic Rayleigh waves (RW) are also present as are the presumed tsunami oscillations beginning at the time indicated by the red arrow "TA" ("Tsunami Arrival"). (c) The high-pass (4 h KB-window) filtered record after suppression of low-frequency oscillations. The Rayleigh waves (RW) are clear and the tsunami waves are also visible (denoted by the red arrow labeled "TA"). High-frequency background noise associated with infragravity (IG) waves, however, still obscure tsunami waves. (d) Clearly discernable tsunami signal, after additional low-pass (6 min KB-window) filtering that suppressed IG-wave and Rayleigh waves. The red solid vertical line labeled "E" denotes the time of the earthquake.

process improves the s/n ratio of the residual series and thus permits continued isolation of the undistorted tsunami waves, but now with much better s/n ratio. The residual (de-tided) time series (Figure 3b) was used in all subsequent analyses.

Low-frequency residual oscillations (Figure 3b) are mainly associated with atmospheric processes and, to some extent, random near-tidal oscillations perennially present in sea level records (cf. Munk et al., 1965). Typical residual amplitudes are ~1.0 cm. After de-tiding, tsunami waves were still not evident in the DART record, but tsunami-like oscillations began to emerge; the beginning of these oscillations is marked with an arrow labeled "TA" (Tsunami Arrival) in Figure 3b. A train of intense high-frequency oscillations caused by the seismic Rayleigh waves (denoted as "RW" in Figure 3b), are noted as having arrived from the source to the DART site approximately 40 min after the main earthquake shock. To further isolate and expose the tsunami waves, high-pass filtering was applied to the residual record with a $\Delta T = 4$ h Kaiser-Bessel window (Thomson & Emery, 2014) to suppress the low-frequency oscillations. Post filtering, record variance dropped to approximately 0.1 cm^2 as compared with the original variance of 361 cm^2. The main features of the filtered record (Figure 3c) were the pronounced train of Rayleigh waves and tsunami waves that arrived at approximately 3:00 UTC, i.e., ~26 h after the earthquake. The numerically computed tsunami arrival time of ~25.8 h following the 2004 earthquake (Figure 1) was in good agreement with the recorded arrival,

High-frequency infragravity (IG) waves are known to be typical features of open ocean records (cf. Rabinovich & Eblé, 2015; Webb et al., 1991). In the last of three time series analysis steps, these waves were suppressed in the high-pass filtered record by applying an additional low-pass filter with a 6 min Kaiser-Bessel window. It was at this point that tsunami waves became visually evident (Figure 3d), highlighting, that in a few consecutive steps, the waves that had been unidentifiable in the original time series (Figure 3a) were presented as distinct tsunami oscillations (Figure 3d). Of note, these analyses steps minimally distorted the actual tsunami signal. Typical amplitude of the measured tsunami waves were 0.5–1.0 cm, while amplitudes of the background oscillations in the tsunami frequency band were considerably smaller: 1.0–1.5 mm (Figure 3d). The resultant s/n ratio confirmed the validity of using the de-tided and twice filtered record for further analysis and characterization of the 2004 tsunami properties.

The similar approach was used to analyse the 15 coastal tide gauge time series recorded during the 2004 event. Residual time series were generated by subtraction of predicted tides were each high-pass filtered using the same 4 h window. The tsunami signal at these shallow stations was amplified relative to deep-ocean locations so the third processing step applied to DART data was unnecessary These filtered series were then used to construct plots of tsunami records for various sites (Figure 4) and to estimate statistical characteristics of the waves. To examine the spectral properties of the tsunami oscillations, we used the unfiltered residual time series. All stations we divided into three groups: (1) "southern" (Figure 4a), (2) "northern" (Figure 4b) and (3) "island" (Figure 4c). This division was partly based on lengths and properties of the records; which is why station Galapagos (Ecuador) was included into Group 2, while Group 3 contained three Chilean island stations: Easter (Pascua), Juan Fernandez and San Felix. Tsunami waves were evident at most mainland stations

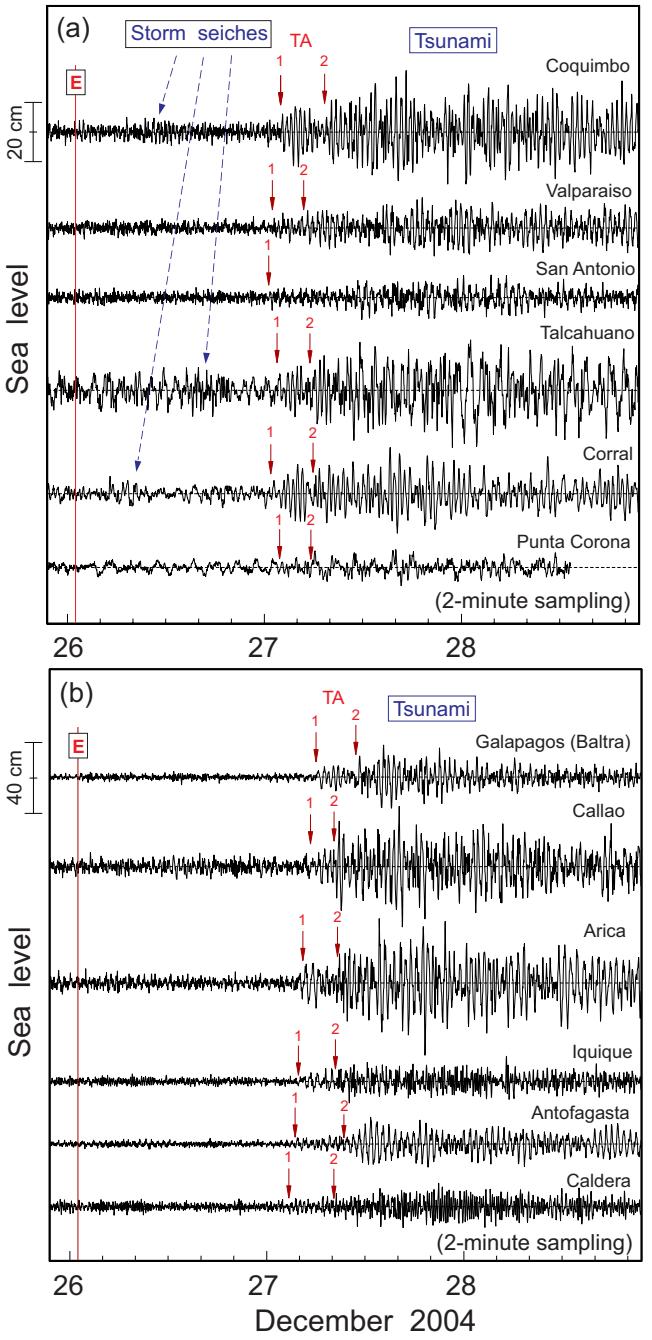

Figure 4. The 2004 Sumatra tsunami recorded by tide gauges along the Pacific coast of South America and nearby island stations. The sampling interval of all records was 2 min. Time series were detided by the least squares method of harmonic analysis and residual time series were then high-pass filtered with a 4 h Kaiser-Bessel (KB) window. The red solid vertical line labeled "E" denotes the time of the earthquake; red arrows labeled "1" and "2" indicate arrivals of the first and second tsunami wave trains. (a) The southern group of coastal stations; dashed long blue arrows denote seiches, associated with atmospheric activity. (b) The northern group of coastal stations. (c) Three island stations located offshore of Chile: (1) the residual high-pass filtered (4 h) records, (2) the same records but after additional low-pass-filtering with 8 min KB-window.

(Figures 4a and 4b) and their arrival times were in agreement with the numerically estimated tsunami travel times (Figure 1). Noticeable seiches, associated with atmospheric activity ("storm seiches") are seen on 26 December in records of Talcahuano, Coquimbo and Corral (Figure 4a), however they are easily recognizable from the incoming tsunami waves. The island records from Group 3 presented a major problem for tsunami analysis (Figure 4c). High-frequency oscillations associated with infragravity waves (produced by nonlinear interaction of storm waves and swell) are very strong at the three stations, while minimal tsunami amplification occurs; an additional low-frequency filtering with various KB windows (from 6 to 20 min) and wavelet analysis (cf. Thomson & Emery, 2014) were used to distinguish and isolate tsunami waves at these stations and to specify main statistical tsunami parameters.

4. Observed Tsunami Parameters

Global tsunami propagation model runs (Kowalik et al., 2007; Titov et al., 2005), showed that 2004 Sumatra tsunami waves entered the southeastern Pacific Ocean from the Indian Ocean, and propagated around Australia and New Zealand along the Southeast Indian Ridge, the Pacific Antarctic Ridge, and the East Pacific Rise (Figure 1). The mid-ocean ridges served as a wave-guide for the 2004 tsunami, efficiently transmitting the tsunami energy from the source area in the Indian Ocean to far-field regions in the Pacific Ocean. The main "eastern" energy flux was directed counterclockwise around the ocean; specifically, this flux transported considerable energy to the coasts of Chile, Peru and Ecuador (cf. Rabinovich, et al., 2006; Rabinovich, Candella, et al. 2011).

Preliminary analyses (Figure 4) indicated that the tsunami wave field in the southeastern Pacific Ocean was much more complicated than in the Indian Ocean (cf. Merrifield et al., 2005; Rabinovich & Thomson, 2007; Rabinovich, Candella, et al. 2011). Examination of these records revealed several common features that were fundamentally different from those in the Indian Ocean. Specifically:

a. Maximum waves in the Indian Ocean occurred near the beginning of the first incoming wave train (first, second or third arriving wave); in contrast, in the southeastern Pacific Ocean (SE Pacific) the largest waves were contained in the second or the third wave train, i.e., 0.3–1 day after the first tsunami arrival.
b. Arrival of tsunami waves in the Indian Ocean was marked by an abrupt and unambiguous change in the record, while in the SE Pacific Ocean, wave arrival was difficult to ascertain as the tsunami tended to be obscured by background noise.
c. Tsunami waves quickly decayed at the Indian Ocean stations, while the typical feature of the SE Pacific Ocean records was tsunami ringing for several days.

All indicated properties of the 2004 tsunami records for the southeastern Pacific were similar to those in the North Pacific and North Atlantic (Rabinovich et al., 2006), potentially reflective of general far-field tsunami behavior.

The basic statistical characteristics of the tsunami waves, including the arrival time, travel time, maximum amplitude, maximum wave height (the maximum of either trough-to-crest or crest-to-trough), and principal wave periods, were estimated at DART 32401 and at all coastal tide

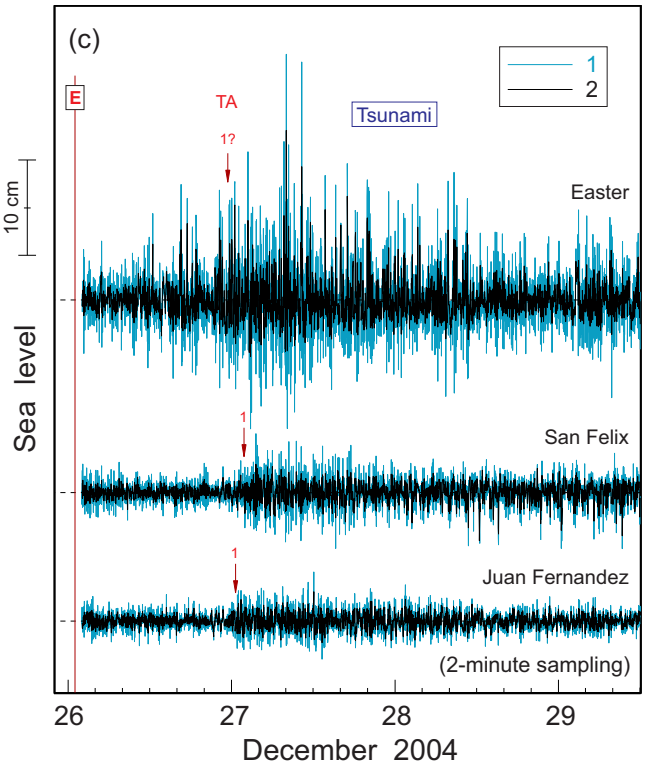

Figure 4. (continued)

gauges available for this study (Table 1). The first 2004 tsunami wave arrived at the location of DART 32401 at 02:54 UTC on 28 December, i.e., 25 h 55 min after the main earthquake shock. Approximately 4 h later, the second wave train arrived with the amplitudes substantially larger than those in the first train. Over the full duration of the event, the largest recorded wave heights were associated with this particular wave train (Figure 5). The maximum wave height of ~2.0 cm occurred at 10:26 UTC on 28 December, or approximately 7.5 h after the first wave arrival. A specific feature of the open-ocean record was the presence of regular, almost monochromatic, oscillations of ~40 min period.

The 2004 tsunami waves that were measured at the mainland coastal stations had much less regular character than at the open-ocean 32401 and were strongly different at different stations. It was, therefore, apparent that local topography and bathymetry played the fundamental role in their formation. The largest oscillations with maximum trough-to-crest wave heights of 72 and 67 cm, were observed at Arica, Chile and Callao, Peru respectively (Table 1 and Figure 4b). The weakest oscillations were recorded at San Antonio (15 cm), Punta Corona (16 cm) and Valparaiso (18 cm), all from the southern group of stations (Figure 4a).

The 2004 tsunami waves arrived at the mainland Chilean coast primarily from the southwest (Figure 1). They arrived first at San Antonio at 00:30 UTC on 28 December (23 h 31 min after the main shock), at Corral at 00:54 UTC (23 h 55 min) and soon after at Valparaiso at 01:00 UTC (24 h 01 min). The waves then propagated northward along the South American coast, reaching Arica at 04:13 UTC (27 h 14 min) and then Callao at 05:46 UTC (28 h 47 min). Finally, at 06:06 UTC tsunami waves arrived at Baltra, Galapagos Is. (29 h 07 min).

A typical feature of almost all coastal records was the second train of waves (indicated in Figure 4 by red arrows labeled as "2") that came 4–6 h later and had higher waves than in the first train. Then several more trains arrived, which were even stronger than the second train (in contrast to what was observed at DART 32401 where the second train was the strongest). Such convoluted wave structure and persistent ringing of coastal records is clearly due to the evolving properties of the wave trains during their trans-oceanic propagation and the resonant properties of coastal topography:

1. Tsunami waves approach any specific site by numerous pathways and after multiple reflections from continental margins and large island groups. Wave trains arriving from various directions superimpose each other in a random way and can create considerable intensification of an arbitrary wave train.
2. Tsunamis in coastal regions are mainly associated with "harbor oscillations," i.e., with eigenmodes generated in bays, harbors and inlets by incoming tsunami waves (Rabinovich, 2009). Arriving tsunami trains keep pumping energy into these resonant oscillations (the "swing effect") and can cause considerable amplification of the signal. This effect is especially important for harbors with high *Q*-factor; Arica and Callao are exactly such sites (in particular, this is evident from the results of spectral analysis of the records at these stations; see section 5.2, Figure 8b), which is why the maximum tsunami wave heights were observed specifically at these stations.

Tsunami detection and estimation of the respective statistical parameters were very difficult for three island stations: Easter, Juan Fernandez and San Felix. The records at these stations were very noisy. It appears that the corresponding tide gauges are strongly affected by intense wind waves, swell, and associated IG-waves. To isolate tsunami waves we used various types of low-frequency filters (Figure 4c). The question, however, remains: how can we separate the IG-waves and high-frequency tsunami waves? As figure 4c shows, our efforts were largely unsuccessful, and the statistical estimates for these three sites are questionable (Table 1). One of the most important but problematic parameters is the exact arrival time of tsunami waves. To specify the arrival times for the island and certain coastal stations we used *f-t* diagrams (section 5.1; Figure 6).

Table 1
Tsunami Characteristics for 15 South American Tide Gauge Stations and DART 32401

			First wave		Maximum wave			
No.	Station	Δt (min)	Arrival time (UTC)	Travel time (h:min)	Amplitude (cm)	Observed time (UTC)	Height[a] (cm)	Observed period (min)
1	*Easter (Pascua) Island (Chile)*	2	01:08[b]?	24:09?	25?	12:02[b]	39?	6
2	*Juan Fernandez Island (Chile)*	2	00:47[b]?	23:48?	5?	16:04[b]	8?	7
3	*San Felix Island (Chile)*	2	02:05[b]?	25:06?	6?	07:34[b]	10?	7
4	Punta Corona (Chile)	2	01:46[b]	24:47	8	15:40[b]	16	25, 130
5	Corral (Chile)	2	00:54[b]	23:55	15	15:20[b]	29	32
6	Talcahuano (Chile)	2	01:38[b]	24:39	20	01:08[c]	42	32, 60
7	San Antonio (Chile)	2	00:30[b]	23:31	8	03:38[c]	15	12, 50
8	Valparaiso (Chile)	2	01:00[b]	24:01	12	14:54[b]	19	33, 40
9	Coquimbo (Chile)	2	02:02[b]	25:03	19	16:02[b]	37	33
10	Caldera (Chile)	2	02:12[b]	25:13	11	20:56[b]	23	17
11	**DART 32401**	**0.25**	**02:54[b]**	**25:55**	**1.0**	**10:26[b]**	**2.0**	**40**
12	Antofagasta (Chile)	2	03:32[b]	26:33	15	12:40[b]	26	44
13	Iquique (Chile)	2	03:44[b]	26:45	13	05:12[c]	24	15
14	Arica (Chile)	2	04:13[b]	27:14	32	19:04[b]	72	36, 48
15	Callao (Peru)	2	05:46[b]	28:47	34	16:08[b]	67	37
16	Baltra, Galapagos Is. (Ecuador)	2	06:06[b]	29:07	19	14:16[b]	35	40

Note. Island Stations are Written in italics. Δt is the sampling rate for the gauge.
[a]Either maximum upcrossing or downcrossing.
[b]28 December.
[c]29 December.

5. Tsunami Analysis

Data recorded at the open-ocean DART station 32401 and the 15 coastal tide gauges were examined by several types of analyses. The main purpose of our investigation was to estimate spectral properties of the observed waves, both near the coast and in the open ocean, examine their time and space evolution and separate the influence of the topography and source characteristics on the parameters of the arriving waves.

5.1. Time-Frequency Analysis

To examine temporal variations of the recorded 2004 Sumatra tsunami waves in the tsunami frequency domain, we used a multiple-filter method, which is similar to wavelet analysis (cf. Thomson & Emery, 2014) and is based on narrow-band filters with a Gaussian window that isolates a specific center frequency, $\omega_n = 2\pi f_n$. This method was effectively used to examine various tsunami events (cf. Rabinovich & Thomson, 2007; Rabinovich et al., 2006, Rabinovich, Stroker, et al., 2011; Thomson et al., 2007); it enables us to determine changes in a tsunami signal as a function of frequency, f, and time, t (so called "f-t diagrams").

An expanded record view and respective f-t diagram for DART 32401 are shown in Figure 5. The plots revealed the abrupt and distinct arrival of tsunami waves. The main tsunami energy was concentrated at periods of 30 to 50 min with a peak period at 40 min. A secondary, weaker frequency band with slightly enlarged energy was at periods 23–27 min. A specific property of arriving tsunami waves, evident in the f-t diagram, was their marked train structure with a typical train length of approximately 4–6 h. The second train ($\sim$4.5 h after the first arrival), as previously mentioned, was the strongest recorded.

Figure 6 presents f-t diagrams for 15 coastal tide gauge tsunami records separated into three groups: southern (Figure 6a), northern (Figure 6b) and island (Figure 6c). In all plots, tsunami arrival times are observed to be well defined and mutually consistent (in good agreement with each other). The same energetic frequency band, as for DART 32401, related to periods of 30–50 min was the dominant feature presented in the majority of plots. A few exceptions in the southern group are worth noting: at San Antonio the peak period was at 50 min, at Talcahuano the peak was at 35 and 100 min, and at Punta Corona, the peak was at 25 and 130 min (Figure 6a). For the northern group of stations, two f-t diagrams are different from the others: Iquique and Caldera; at both stations the main energy is concentrated at relatively high frequencies

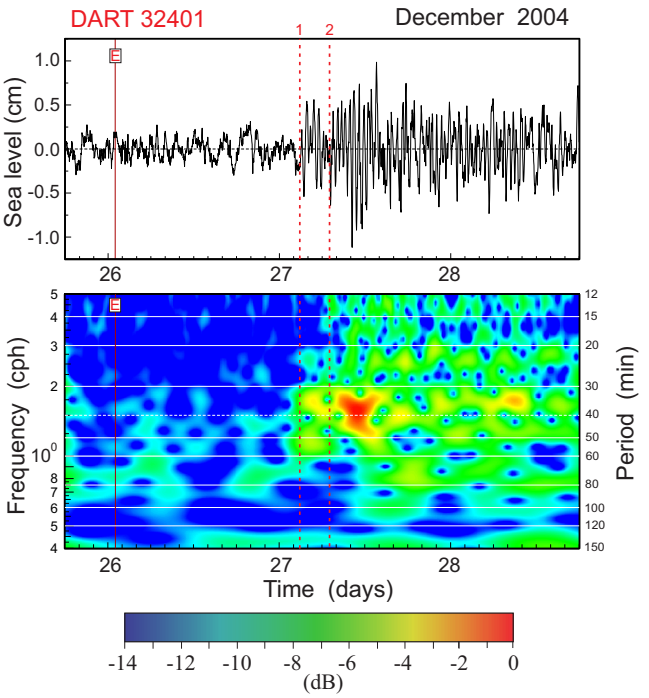

Figure 5. (a) The DART 32401 filtered record with the isolated 2004 tsunami and (b) its frequency-time (*f*-*t*) wavelet diagram. The red solid vertical line labeled "E" denotes the time of the earthquake; the vertical red dashed lines labeled "1" and "2" indicate arrivals of the first and second wave trains.

of 4–5 cph (periods 12–15 min), while at lower frequencies of 1–3 cph (periods 20–60 min) the tsunami oscillations are noticeably weaker (Figure 6b).

The *f*-*t* diagrams for three island stations (Figure 6c) are similar to each other but dissimilar from those for the mainland stations and Galapagos Is. (Figures 6a and 6b). The first arrivals are recognizable in the figure, but they are not as evident as at the stations from the southern and northern groups. The tsunami signals present as chaotic, possibly due to a high noise level. At these stations, there are no obvious energetic frequency bands, with the possible exception of San Felix where there is a visible increase of energy at 30–50 min. In general, the island stations have relatively more energy at higher frequencies. The plots indicate a clear train structure for the tsunami waves with typical train duration of 6–10 h.

5.2. Spectral Analysis

Wavelet analysis provides a means to estimate the nonstationary properties of tsunami waves and their evolution in time, while spectral analysis serves to evaluate the general frequency content of the recorded waves, and to relate this content to the tsunami source and resonant features of the corresponding site. The observed spectrum, $S_{\mathrm{obs}}(\omega)$, during a tsunami event can be presented as superposition of the tsunami, $S_{\mathrm{tsu}}(\omega)$, and background, $S_{bg}(\omega)$, spectra,where ω is the angular frequency. In practice, we do not know the exact background spectrum during the event, but we can assume that it is approximately the same as before the event.

To examine the spectral properties of tsunami oscillations during the 2004 tsunami and to compare these properties with those of the background oscillations at the same sites, we separated the records into two parts: tsunami and pre-tsunami. The time period preceding the tsunami arrivals (preceding the earthquake for DART 32401 to avoid the influence of Rayleigh waves) was identified as "normal" and used for analysis of the background signal. For the open-ocean station, which has the sampling interval $\Delta t = 15$ s, we chose a time period of 5.33 days (30,720 points) for spectral analysis of the background and 1.07 days (6,144 points) for the tsunami; for the coastal stations ($\Delta t = 2$ min), which had much shorter pre-tsunami series, we used the same length of 1.07 days (768 points) both for the background and tsunami analysis.

The spectral analysis procedure followed was similar to that described by Thomson and Emery (2014) (see also, Rabinovich & Thomson, 2007; Rabinovich et al., 2006). To improve the spectral estimates, we used a Kaiser-Bessel (KB) spectral window with half-window overlaps prior to the Fourier transform. The length of the window was chosen to be $N = 2048$ for DART 32401 and $N = 256$ for coastal stations (512 min for both types of records) yielding $\nu = 58$ degrees of freedom for the background DART spectrum and $\nu = 10$ for the tsunami DART and all coastal spectra. The spectral resolution was $\Delta f \approx 0.117$ cph and the Nyquist frequency $f_n = 120$ cph for DART and $f_n = 15$ cph for tide gauge records. The computed tsunami and background spectra for DART 32401 are shown in Figure 7a and for coastal stations in Figures 8a–8c.

Spectral analysis of the open-ocean record (Figure 7a) shows that the background spectrum decrease monotonically with frequency ω as ω^{-2}, typical for the longwave spectra in the open ocean (cf. Kulikov et al., 1983; Rabinovich, 1997). A "hump" at frequencies 10–50 cph is artificial: a general increase at frequencies higher than 6 cph is associated with influence of infragravity (IG) waves generated by the nonlinear interaction of wind waves and swell (cf. Aucan & Ardhuin, 2013); however, at higher frequencies (>20 cph) the recorded waves began to attenuate very fast because of the nonhydrostatic nature of the bottom pressure response at these frequencies (cf. Rabinovich & Eblé, 2015). The tsunami spectrum matches the background spectrum at low and high frequencies, while at intermediate frequencies they have a prominent "bulge" associated with the tsunami energy. The tsunami energy spans the band of approximately 0.25 to 10 cph (periods from 4.0 h to 6 min). The peak value is at frequency of 1.5 cph (40 min). In general, the 2004 Sumatra tsunami spectrum at DART 32401 looks similar to those at DART 46405 and NeMO, except that the peak value at 46405 was at 50 min (Rabinovich & Eblé, 2015; Rabinovich, Stroker, et al., 2011). Because the

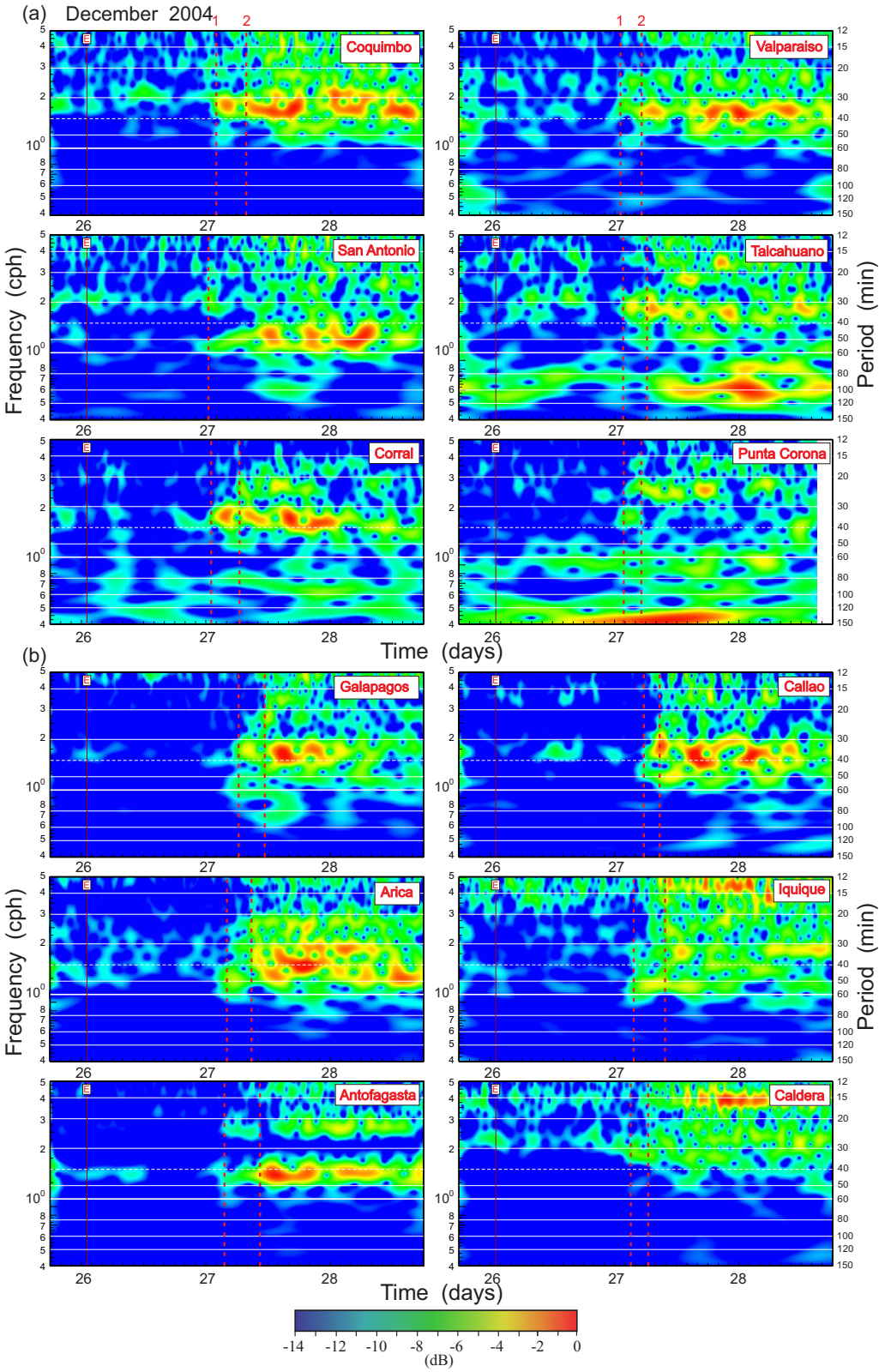

Figure 6. Frequency-time (*f-t*) wavelet diagrams of the 2004 Sumatra tsunami in coastal records. The red solid vertical line labeled "E" denotes the time of the earthquake; the vertical red dashed lines labeled "1" and "2" indicate arrivals of the first and second wave trains. Wavelet plots are grouped as (a) The southern stations; (b) the northern stations; and (c) the three island stations offshore of Chile.

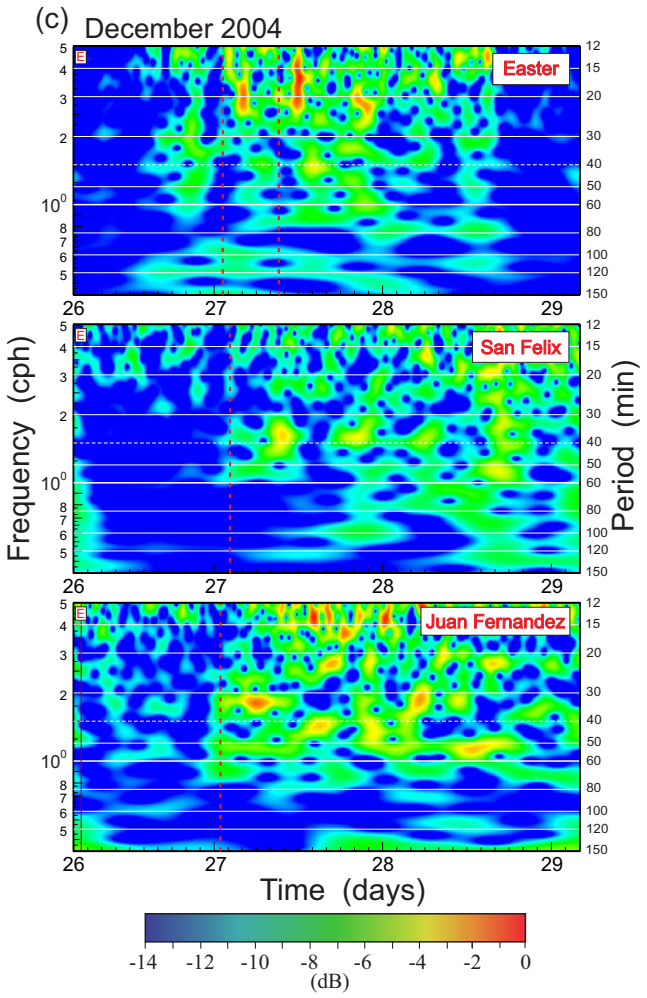

Figure 6. (continued)

open-ocean spectra are not affected by coastal and shelf effects, $S_{tsu}(\omega)$ at DARTs 32401, 46405 and NeMO presumably largely reflect the properties of the 2004 Sumatra source region with the long tsunami wave periods associated with the large initial source extension of about 1,300 km (Stein & Okal, 2005).

In comparison with open-ocean spectra (Figure 7a), the coastal spectra are more "jagged," strongly variable from one station to another, and characterized by marked spectral peaks. The spectral structure of coastal tsunami and background oscillations mainly reflects the individual local resonant properties of particular sites. At the same time, a specific peak with a period of 37–39 min is a dominant spectral feature at several stations: Coquimbo, Valparaiso and Corral (Figure 8a), Arica, Callao and Galapagos (Figure 8b), San Felix (Figure 8c). A peak with a close period of 43 min is observed at Antofagasta (Figure 8b) and Juan Fernandez (Fig. 8c). The topographic influence on formation of these peaks is obvious because at most stations they appear both in the tsunami and background spectra. However, undoubtedly strong amplification of the respective oscillations during the tsunami event has a resonant nature and is associated with the 40 min tsunami peak observed in the open ocean (Figure 7).

In addition to the mentioned peaks, there are some other prominent peaks, salient at some sites and clearly present in the wavelet analysis of section 5.1: 49 min at San Antonio, 100 and 34 min at Talcahuano, 24 min at Punta Corona (all Figure 8a), 23 min at Antofagasta and 16 min at Caldera (Figure 8b). In general, the spectra for both the tsunami and background records are "red," with spectral energy decreasing with increasing frequency. The exceptional are spectra of the three island stations shown in Figure 8c that become "blueish" (increasing with frequency) at frequencies higher than 3 cph (at periods shorter than 20 min). This is probably due the influence of infragravity waves (cf. Rabinovich & Eblé, 2015) affecting the open coasts of these islands (Easter, San Felix and Juan Fernandez). At most stations, the difference between the tsunami and background spectra is considerable, demonstrating that the 2004 Sumatra tsunami even 18,000 km from the source was still substantial.

5.3. Spectral Ratios

Because of the strong influence of local topography on tsunami waves arriving at the coast, it is recognized as being difficult to reconstruct characteristics of the source region based solely on data from coastal tide gauges (cf. Bernard et al., 2001; Mofjeld, 2009). Rabinovich (1997) suggested a method to bypass this problem and separate the influences of topography and source on the observed tsunami spectra. The method is based on the assumption that the topographic transfer function, $W(\omega)$, describing the linear transformation of long waves approaching the coast,

$$S(\omega) = W(\omega)\, E(\omega), \tag{1}$$

is the same for tsunami waves and ever-present background long waves. Consequently, we can assume that individual characteristics of the observed spectra at the jth site are related to the site-specific topographic function, $W_j(\omega)$, while general properties of these spectra are associated with the tsunami source. The ratio,

$$R^j_s(\omega) = S^j_{tsu}(\omega) / S^j_{bg}(\omega), \tag{2}$$

of the tsunami to the background spectrum suppresses the local topographic influence and enable us to obtain a function that is determined almost entirely by the external forcing (i.e., by the characteristics of the open-ocean tsunami waves). Taking into account (1)-(2), we can specify the "spectral source function,"

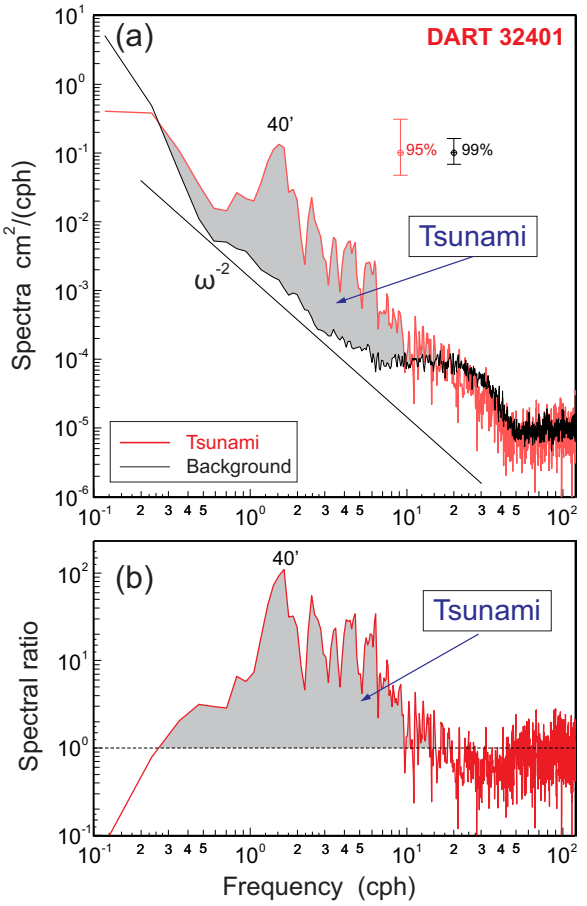

Figure 7. (a) Spectra of the background (pre-tsunami) and the 2004 Sumatra tsunami oscillations recorded in the southeastern Pacific at DART 32401. The spectral "hump" associated with the tsunami energy is shaded; a reference power law ω^{-2} is denoted. Also shown are the 95% (for tsunami) and 99% (for background) confidence levels. (b) The tsunami-to-background spectral ratio "source function" for this record.

i.e., the "spectral ratio" that quantifies the amplification of the tsunami spectrum relative to the background conditions:

$$R_j(\omega)=\frac{S^j_{\mathrm{obs}}(\omega)}{S^j_{bg}(\omega)}=\frac{\left[E^j_{\mathrm{tsu}}(\omega)+E^j_0(\omega)\right]}{\hat{E}^j_0(\omega)}\approx R^j_s(\omega)+1.0. \quad (3)$$

where we can assume that the open-ocean background spectra before and during the event are approximately equal: $\hat{E}^j_0(\omega)\approx E^j_0(\omega)$. The individual spectral ratio function at the jth site, $R_j(\omega)$, is presumed to be an invariant characteristic of the source and is, therefore, expected to be similar at all stations. The similarity of the function $R_j(\omega)$ at various stations validates the initial assumptions. The high efficiency of this method has been demonstrated for many tsunami events (cf. Rabinovich, 1997; Shevchenko et al., 2013; Vich & Monserrat, 2009; Zaytsev et al., 2016, 2017).

Figure 7b presents the spectral ratio (proxy source function) for the 2004 Sumatra tsunami recorded at DART 32401. This function enables us to specify the exact frequency band of the 2004 tsunami in the open ocean: it spans from 0.25 to 15 cph (periods from 4 h to 4 min). The ratio has a characteristic "triangle-like" shape with a peak value at frequency 1.5 cph (period of 40 min). The gradual decrease of $R_j(\omega)$ at frequencies higher than the peak value is broken by a few significant troughs, the largest of which (with a drop of 1.5 orders) is at frequency ~2.0 cph (30 min).

In general, the spectral tsunami ratios for coastal stations (Figure 9) have a similar "triangle" shape with a peak value at ~1.5 cph (40 min) and occupy approximately the same frequency band of 0.25 – 15 cph as for DART 32401 (Figure 7b). It is especially interesting that they have very similar "troughs." In particular, the main "trough" at 2 cph (30 min) has an apparent association with some spectral properties of the source area. The differences in $R_j(\omega)$ estimated at various stations are partly related to the short pre-tsunami series length and insufficient number of degrees of freedom for computed background spectra, $S^j_{bg}(\omega)$ (the denominator in expression (3)). However, overall, the spectral ratios are much more similar than individual spectra at the same sites, which have specific peaks related to coastal topographic resonance. In $R_j(\omega)$ such peaks are absent. The coastal spectra are more "jagged," strongly variable from one station to another, and characterized by marked spectral peaks.

6. 2004 Sumatra Tsunami Modeling

Several numerical studies have been conducted for the 2004 Indian Ocean tsunami (cf. Fujii & Satake, 2007; Kowalik et al., 2005, 2007; Titov et al., 2005). Model simulations of this event fall, roughly, into two main groups differentiated by scope: (1) reconstruction of the tsunami source; and (2) modeling the tsunami impact on Indian Ocean coastlines. Both simulation efforts use various data to constrain the model and to validate model predictions. These models have been focused on highly impacted areas in the Indian Ocean, whereas the available tsunami observation data were from coastal tide gauges that mostly had limited accuracy and insufficient time resolution (from 2 to 15 min). While the tide gauge data were important for early modeling studies aimed at estimating the 2004 Sumatra tsunami source model (cf. Fine et al., 2005; Fujii & Satake, 2007), these data proved inadequate information for more sophisticated tsunami investigations due to sparse coverage, high background noise and infrequent sampling intervals (see Satake & Kanamori (1991) for discussion of these problems). The record from Chilean DART 32401 is one of the few deep-ocean high-resolution records of this tsunami in general, and the only one in the South Pacific. However, in order to be of use for comparison and validation of numerical models, such models would require running a global propagation simulation for an unprecedentedly long time.

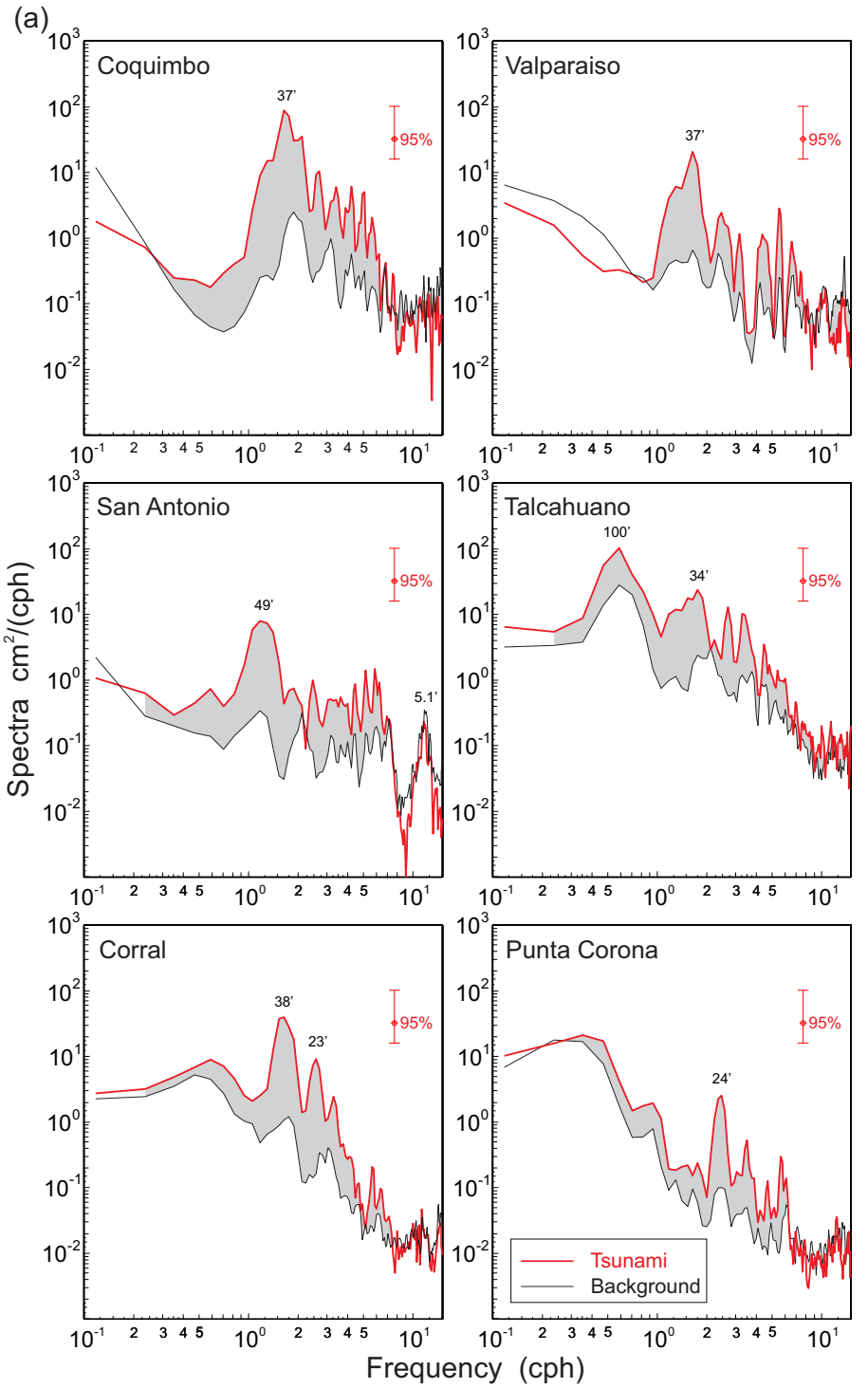

Figure 8. Spectra of the background (pre-tsunami) and the 2004 Sumatra tsunami signal recorded at coastal tide gauges along the Pacific coast of South America for the group of (a) southern stations; (b) northern stations; and (c) the three island stations offshore of Chile. The shaded areas denote the tsunami energy. The 95% confidence level is shown on the upper right inside each plot frame.

The tsunami source and the modeling technique used for the present numerical computation of the global 2004 tsunami propagation was the same as in the model of Titov et al. (2005). The source parameters of the model were constrained based on altimetry tsunami measurements in the Indian Ocean and seismic

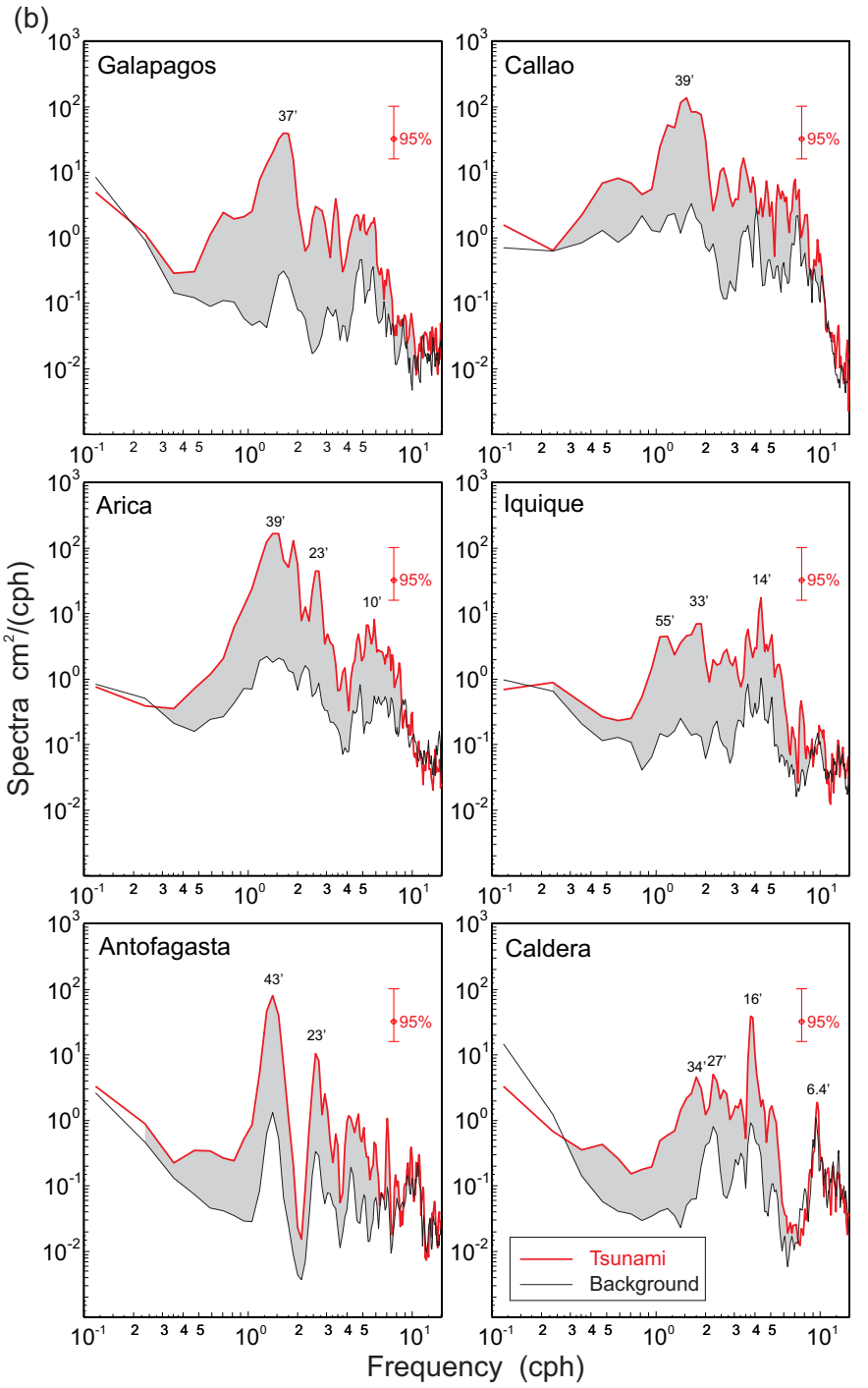

Figure 8. (continued)

analysis of the event (Smith et al., 2005; Titov et al., 2005). Previous studies showed good qualitative agreement of the model with the observed 2004 tsunami parameters (cf. Candella et al., 2008; Geist et al., 2006; Rabinovich, Woodworth et al., 2011; Thomson et al., 2007). The goal of the current modeling was not to improve the source model, but rather, to estimate its accuracy and to test the predictive limits of the tsunami modeling. The open-ocean and coastal data were used as an independent criterion of the model reliability and to acquire important additional information about the global 2004 Sumatra tsunami wave field.

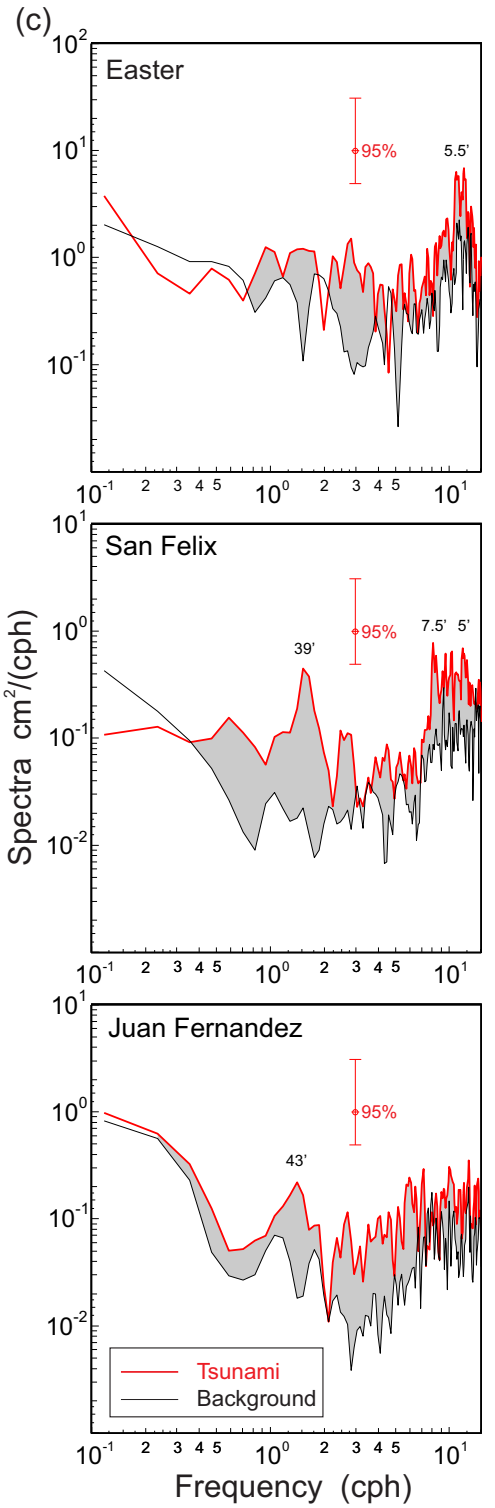

Figure 8. (continued)

The numerical analysis of distant tsunami records with wave arrival times that ranged from 24 to 29 h after the main earthquake shock required a much longer than usual simulation of tsunami propagation. The original simulated series of Titov et al. (2005) were extended in time from 32 h to over 72 h making it possible to numerically compute 3 days of tsunami travel across the oceans and to obtain long simulated records at far-field sites for direct comparison with actual DART and coastal tsunami records. To date, this appears to be the longest tsunami propagation modeling comparison involving remote measurements. The results showed that tsunami waves detected at DART 32401 propagated some 18,000 km, or half the circumference of Earth to reach this site.

Figure 10 shows snapshots of the 2004 tsunami wave field in the southeastern Pacific Ocean. Waves from the source in the Indian Ocean entered the region from two contrasting directions. The "Pacific" wave approached from the west after originally propagating southeastward from the source area near Sumatra; subsequently, upon entering the Southern Ocean, the tsunami waves passed between Australia and Antarctica and then circumnavigated New Zealand before crossing into the South Pacific Ocean and continuing east toward South America. The "Atlantic" tsunami approached from the east after propagating southwestward from the source across the Indian Ocean to the Southern Ocean and continued around South Africa; it moved across the South Atlantic Ocean, and finally entered the Pacific Ocean through the Drake Passage between Antarctica and South America (Figure 10). Thus, the study region is the area of convergence of two global tsunami waves that propagated in opposing directions from the same source and entered into this region almost simultaneously.

The Drake Passage played a particularly important role in formation of the tsunami wave field in the region under study. The National Oceanography Centre, Liverpool (previously the Proudman Oceanographic Laboratory) had two BPRs, with 15 min sampling rates, working in the Drake Passage during the 2004 event. Rabinovich, Woodworth, et al. (2011) used these data and the global tsunami MOST model of Titov et al. (2005) to examine specific properties of the 2004 tsunami waves that propagated through the Drake Passage and entered into the Pacific from the Atlantic Ocean. Atlantic tsunami waves were found to interact with island chains and were scattered by coastal and bottom irregularities and cross-passage fractures leading to a rather complicated wave structure. Despite the complexity of tsunami waves in the vicinity of the Drake Passage and the long sampling interval, data at the two stations; DPN (northern BPR) and DPS (southern BPR), were consistent with numerically computed tsunami waveforms. Specifically, Rabinovich, Woodworth, et al. (2011) found that the simulated waves arrived only 10 min earlier at the location of southern DPS and 15 min earlier at the location of northern DPN than actually measured. Overall, the time differences were less than 1.3% of the total propagation time to the stations.

Computational results of the present study, when coupled with those of Rabinovich, Woodworth, et al. (2011), indicate that the "Atlantic" tsunami wave reached the Pacific southernmost coast of South America (Tierra del Fuego) before the "Pacific" tsunami but propagation through the Drake Passage significantly attenuated the wave (Figure 10a). Model simulations showed that the "Pacific" wave overtook the propagating "Atlantic" wave front and reached all tide gauge sites first (Figures 10b–10d). Therefore, the leading positive wave recorded at all sites is related to the Pacific wave, while contributions from Atlantic approaching waves followed shortly after (Figures 10e, 10f, 11a, and 12).

According to observations (Table 1), the "Pacific" tsunami wave arrived at DART 32401 at 02:54 UTC on December 27, 2004 (25 h 55 min after the main earthquake shock). Snapshots shown in Figures 10d and 10e validate that the numerical outcomes of the model are in good agreement with observations. The numerical simulated record for location of DART 32401 was directly compared with the actual site record. Figure 11a demonstrates that despite the great distance from the

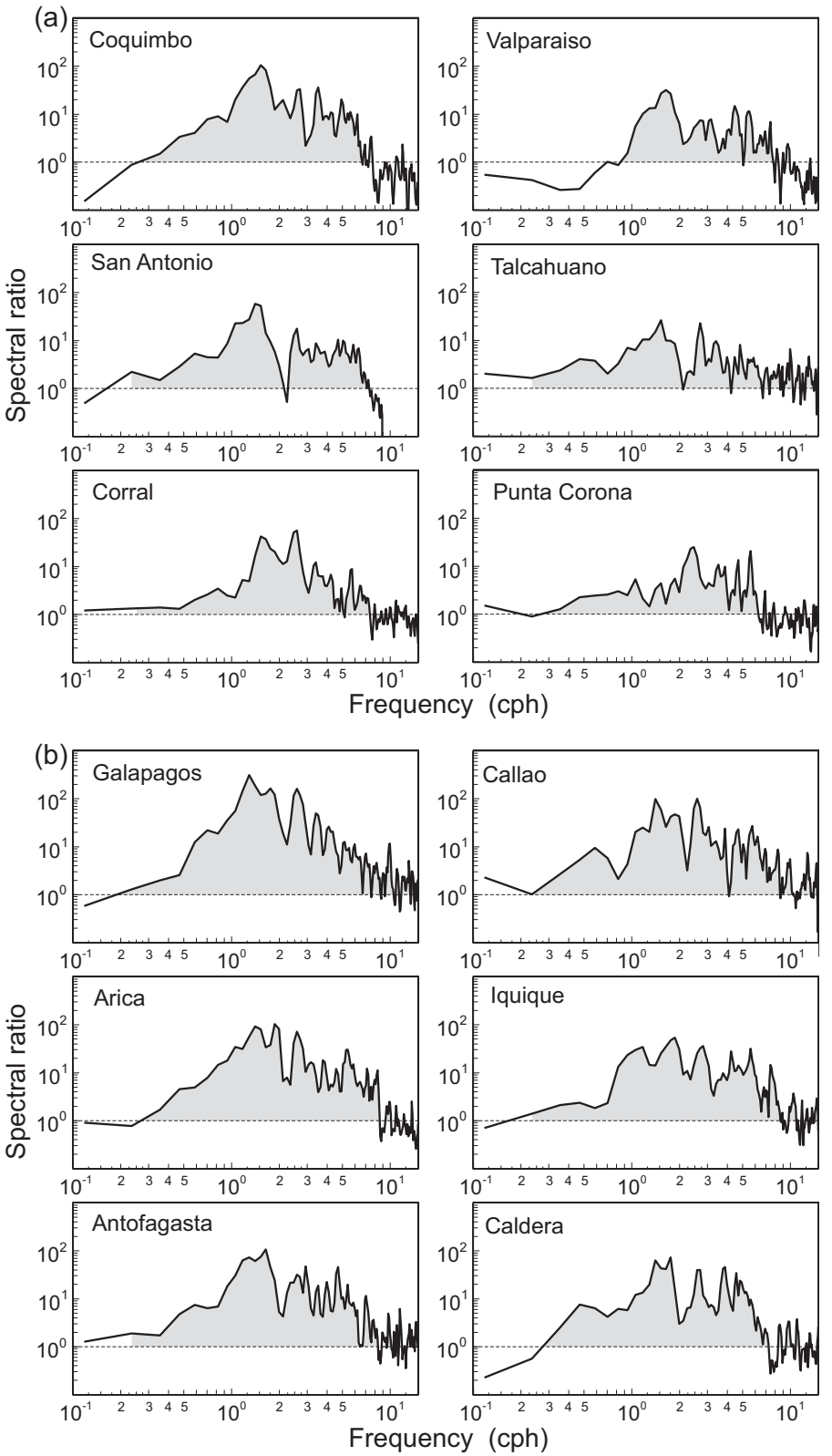

Figure 9. Estimated tsunami/background spectral ratios for the coastal tide gauge spectra shown in Figure 8. Shaded areas denote the tsunami response associated with the arriving waves; i.e., the amplification of the spectra due to the tsunami waves relative to the background spectra for (a) the southern group of stations; (b) the northern group; and (c) the three island stations offshore of Chile.

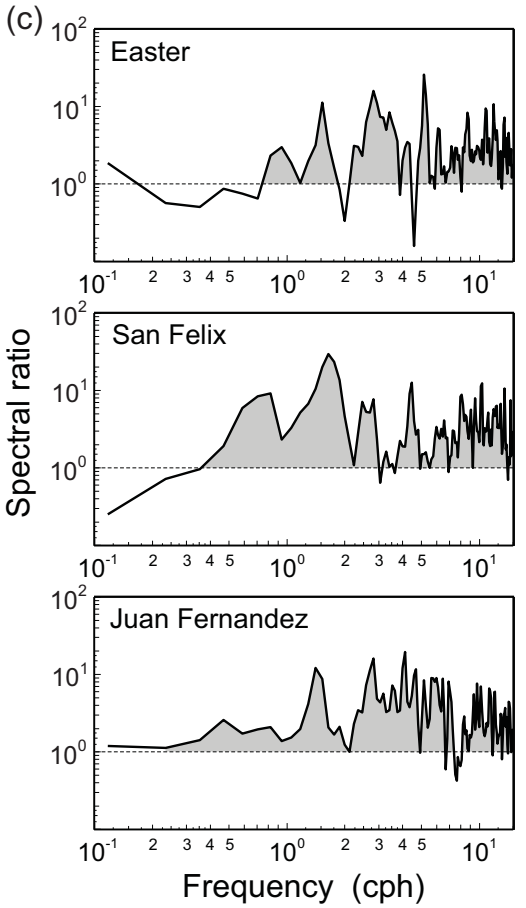

Figure 9. (continued)

source area (~18,000 km), the simulated record matches the observed oscillations at the DART. This appears to have been one of the first examples of the comparison of model results with data from so distant open-ocean instrument. A comparison of the simulated and observed records indicates that the simulated tsunami at DART 32401 was approximately 20 min ahead of the actually recorded, i.e., less than 1.3% of the propagation time. This is approximately the same travel time error as was obtained by Rabinovich, Woodworth, et al. (2011) for the Drake Passage.

Incorporation of the 20 min time shift discussed above did not distort the structure of the simulated tsunami waveforms. The numerically computed tsunami wave trains perfectly coincided in both phase and amplitudes with the observed wave trains. Results of the numerical modeling reproduced accurately the general structure of the observed waves at DART 32401 (Figure 11a). A comparison of computed and observed spectra at this site were found to be consistent (Figure 11b). The main difference was noted at low frequencies (0.2 – 1.0 cph) where the computed spectrum is noticeably larger than the observed one. This is a possible indication that the effective extension of the source area was actually shorter than was assumed for the modeling. According to Fine et al. (2005) (see also Chlieh et al., 2007; Fujii & Satake, 2007; Ishii et al., 2005), the dominant 2004 tsunami waves that propagated throughout the world oceans, was related to the "southern source region," which estimated to be 600–650 km with a "hot spot" of 300–350 km.

An additional computation was done to simulate the tsunami waveforms at coastal sites. To increase accuracy, the results of the low spatial-resolution global propagation model served as input for a telescoping multigrid MOST model run with a set of progressively higher resolution numerical grids at each tide gauge location. The same methodology is employed in the NOAA tsunami inundation forecast. Thus, this comparison not only provided the high-resolution simulations needed for direct comparison with coastal Chilean tide gauges, but also served to test the validity of exceedingly long tsunami propagation forecast capabilities. It is important to note that the coastal modeling conducted for this study used preliminary (unverified) coastal bathymetry data. High-quality fine resolution bathymetry was available only for the Galapagos tide gauge site; for all other locations, nested model grids were constructed with generic bathymetry data compiled and interpolated from the GTOPO30 global data set (https://lta.cr.usgs.gov/GTOPO30) and the SRTM90 data set (http://www.cgiar-csi.org/data/srtm-90m-digital-elevation-database-v4-1). The nested grids are forced with a global grid, and increase resolution in three steps (4 arc-min, 30 arc-sec, and 12 arc-sec) to the inundation grid of ~2 arc-sec, where the gauge location is output. A detailed account of this technique is available in Titov, Kânoğlu, et al. (2016). The accuracy of near-shore and coastal bathymetry data is the most important factor for accurate prediction of the coastal impact of tsunami. While unverified near-coast bathymetry used for this study produced uncertainty in the model results, the high-resolution modeling would allow more realistic estimates of coastal tsunami dynamics and local topographic amplification as compared with low-resolution propagation runs.

In general, numerical results (Figure 12) proved to be better than expected. The simulated wave train structure, tsunami amplitudes, arrival times, and main wave frequencies at most sites coincided well with counterpart tide gauge tsunami waveforms. There were only a few exceptions. The main differences were seen at Punta Corona (Figure 12a), a station with very complicated topography that was probably not adequately accounted for in the constructed model grid. At some stations, in particular at Corral and Valparaiso (Figure 12a), Caldera and Antofagasta (Figure 12b), the model compared well with the first 12–15 h of the observed records, but then the computed and observed records began to diverge. Such differences appear to be related to far-field topographic features responsible for formation of reflected wave trains that approached the coast of Chile long after the first wave arrival.

Maximum tsunami wave height is the easiest local measure of the tsunami energy for a specific site; it is also one of the most important parameters for tsunami forecast. For this reason, the distribution of the maximum 2004 tsunami wave heights (the maximum of either trough-to-crest or crest-to-trough) along the coast of South America was computed and compared with observed heights (Figure 13). There were

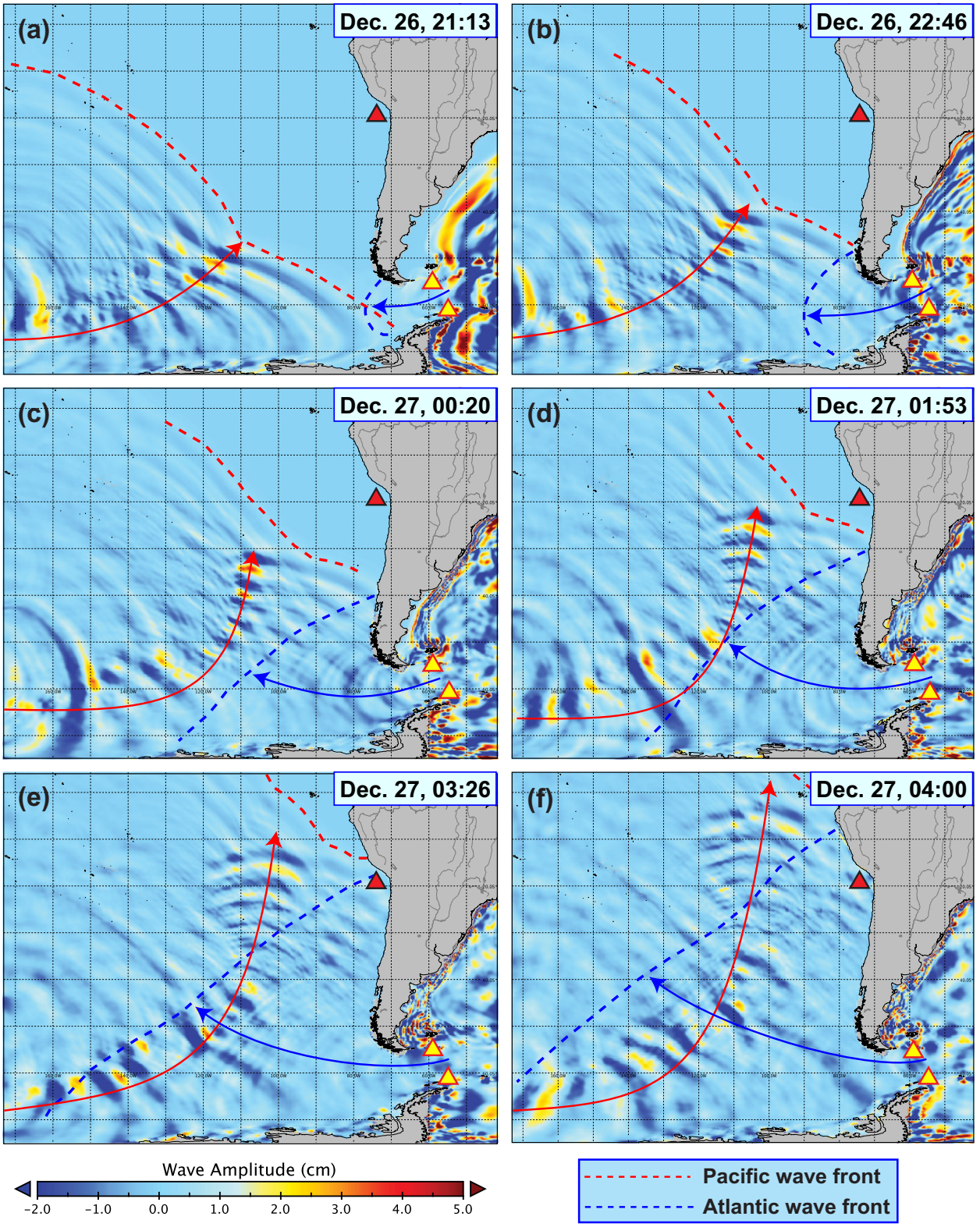

Figure 10. Snapshots in model computation of the 2004 Sumatra tsunami waves propagating into the southeastern Pacific Ocean. Two waves are shown entering the region almost simultaneously: (1) the "Atlantic wave" indicated by the blue arrow (direction) and the blue dashed line (wave front) that propagated from the source area southwestward and arrived at the region from the Atlantic Ocean through Drake Passage, and (2) the "Pacific wave" (red arrow and dashed line) that initially propagated southeastward and then around Australia and New Zealand to arrive at the region and meet the Atlantic wave. The red triangle denotes the location of DART 32401 offshore of Chile. Two yellow red-bordered triangles show the locations of UK BPRs deployed in Drake Passage.

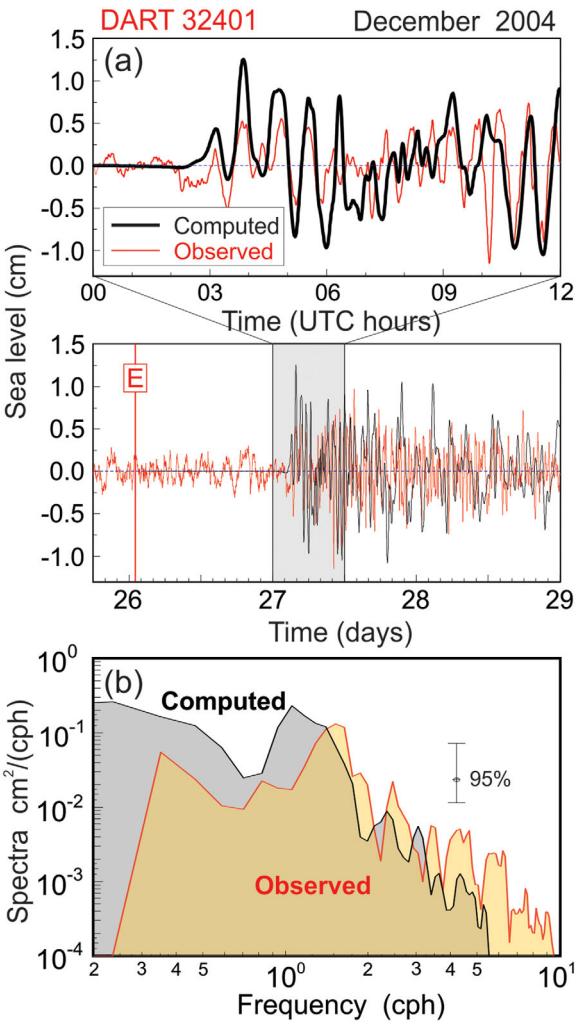

Figure 11. (a) Computed (black) and observed (red) 2004 tsunami waveforms at DART 32401 offshore of northern Chile. Note that the computed record is 20 min offset in time to best fit the data. The red solid vertical line labeled "E" in the lower panel denotes the time of the earthquake. (b) The spectra of the respective records with shown 95% confidence level.

favorable agreements at most stations, with differences <15%. The exceptionally large differences noted at Valparaiso, Caldera, and Antofagasta were caused by intense late-arriving tsunami wave trains (>15 h after the first arrivals) that, as was mentioned earlier, were not reproduced well enough by the model.

Figure 10 suggests that the "Pacific" and "Atlantic" wave trains arriving at southern locations appear to have comparable amplitudes, which effectively may have doubled the tsunami wave heights along this coast. The relative amplification of the wave heights at Talcahuano and Coquimbo (Figures 12a and 13) were probably the manifestation of this combination effect. However, the intensity of both wave trains near the southern end of South America was small, quite possible due to the fact that much of the "Pacific" tsunami energy propagated along the East Pacific Rise, as described by Titov et al. (2005) and is evident in Figure 10. The "Atlantic" wave had larger amplitudes before entering the Pacific, but tsunami waves were dissipated, reflected, and scattered during propagation through the complex bathymetry of the Drake Passage.

7. Discussion

The 2004 tsunami waves propagated nearly half the circumference of the Earth to reach the southwestern coast of South America. Along the way, the waves reflected from many coastal features and topographic elements, were scattered by depth irregularities, and were affected by various atmospheric processes significantly distorting the initial signal. Near the coast, the tsunami waves were strongly modified by the continental slope, shelf and local embayments. Consequently, as is well known, the seafloor topography strongly determines the characteristics of coastal tsunami records. Two natural questions that arise are:

1. Do coastal records still contain information about the initial source?
2. Can we use remote open-ocean and coastal records to obtain spectral characteristics of the source?

The tsunami spectra shown in Figure 8 mainly mirror the individual resonant features of specific sites rather than the spectral characteristics of the source. The approach proposed by Rabinovich (1997) enables suppressing the local bathymetric and topographic influence. Spectral ratios tsunami/background ("source functions"), $R_j(\omega)$, estimated for specific coastal sites (Figure 9), have evident similarity and appear to reflect the essential source properties. However, $R_j(\omega)$, is a stochastic function that depends on various random factors and characteristics of the local background noise, in particular on the consistency of the noise spectrum before and during the event. Also, the observed spectrum, $S^j_{obs}(\omega)$, that is the numerator of expression (4), at certain sites markedly depends on the direction of incoming tsunami waves. To improve the reliability of the source function estimates and to increase the number of degrees of freedom, we can average $R_j(\omega)$ for any group of N stations, viz.,

$$\hat{R}(\omega)=\frac{1}{N}\sum_{j}^{N}R_j(\omega), \tag{5}$$

where $\hat{R}(\omega)$ is the "mean spectral ratio." We assume that the averaging allows us to suppress individual random outliers of $R_j(\omega)$ and to reveal the general properties of these functions. The results of such averaging for two groups of coastal stations, southern and northern, are shown in Figures 14a and 14b, respectively. For comparison, in Figure 14c we also show the spectral ratio for DART 32401 constructed for the same frequency band of 0.1–15 cph. Spectral characteristics at this station are not affected by shelf and coastal topographic effects, thus the corresponding spectral ratio at this site may be considered as the most reliable.

The encouraging result is that the three spectral ratios, two mean ratios for the southern and northern groups of stations and the ratio for DART 32401, are in very good agreement (Figure 14). All main features

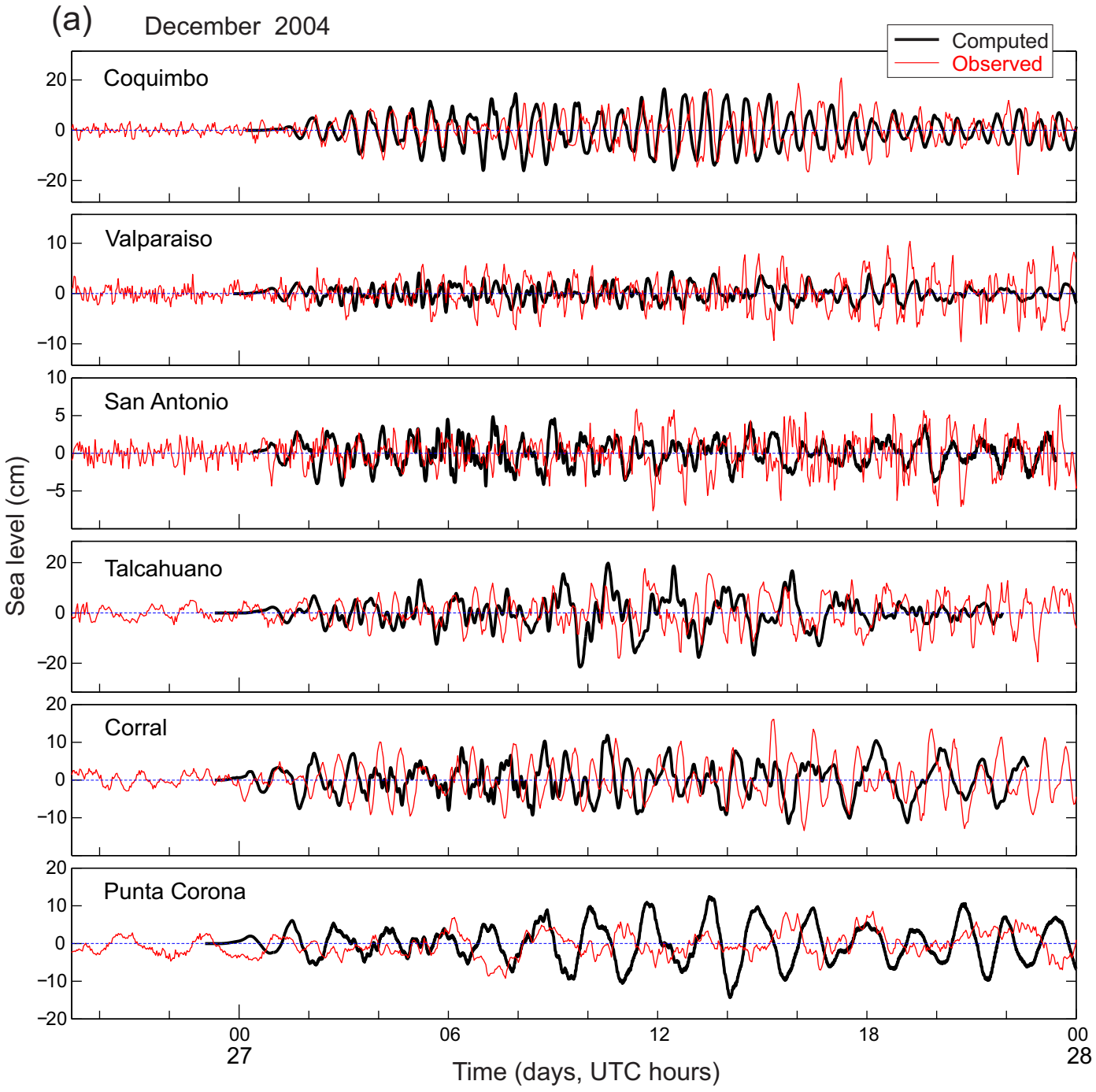

Figure 12. Computed (black) and observed (red) 2004 tsunami waveforms at tide gauge stations along the Pacific coast of South America. Computed time series are shifted back in time by 20 min, as determined by comparison with DART 32401. Stations are grouped as (a) the southern stations; (b) the northern group.

coincide: the general triangle shape of the ratios, the tsunami frequency band of 0.25–10 cph (periods from 4 h to 6 min), and even the two most prominent ratio peaks at periods 40 and 23 min. The absolute values of $\hat{R}(\omega)$ for the northern stations are a little higher than for the southern stations, in accordance to noticeably larger tsunami heights at the former stations probably due to their proximity to the East Pacific Rise, i.e., to the main path of the propagating Pacific tsunami wave (Figures 1b and 13). However, in general, all three discussed ratios are of the same order.

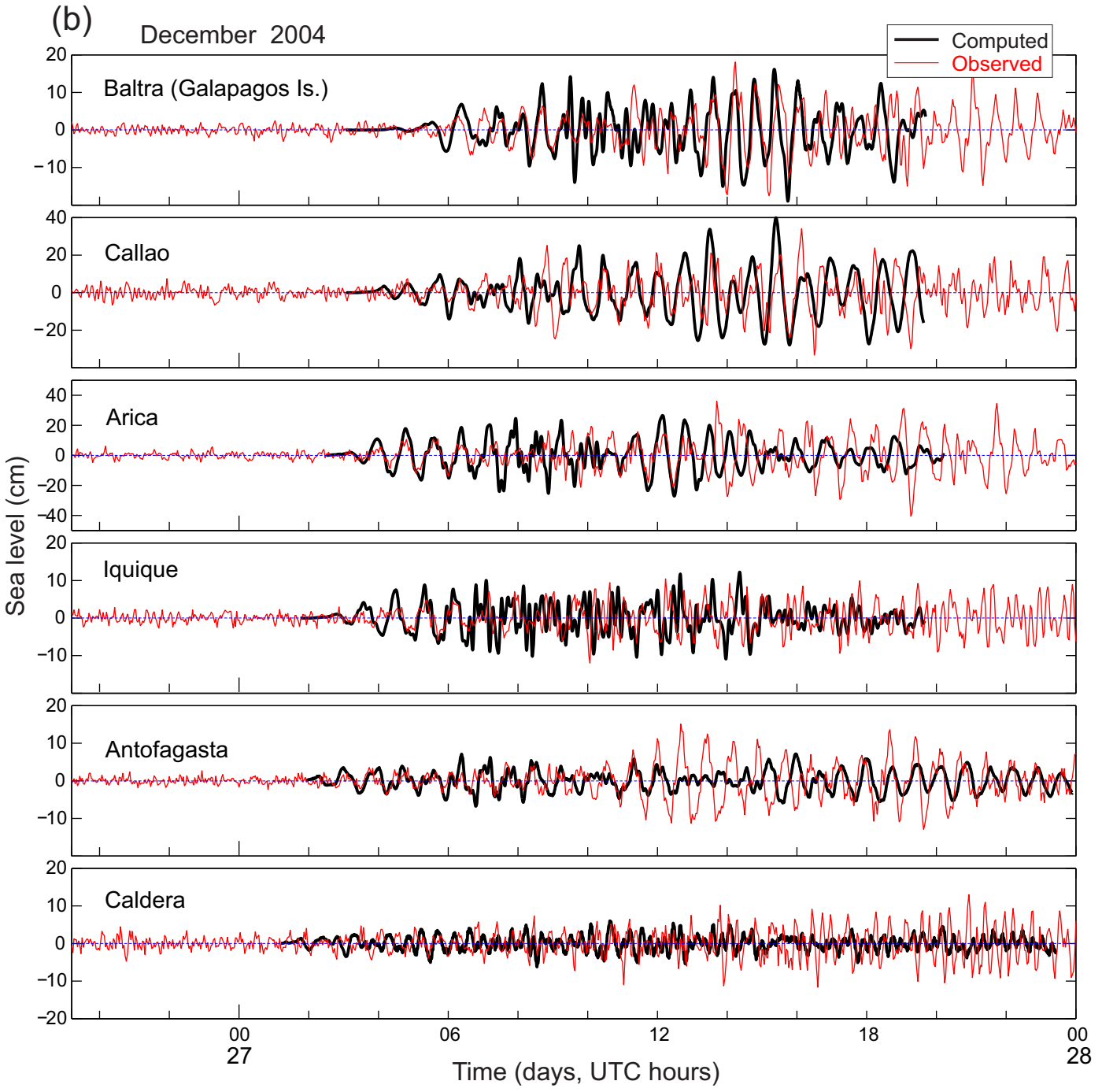

Figure 12. (continued)

Zaytsev et al. (2016, 2017) recently demonstrated that the mean spectral ratio $\hat{R}(\omega)$ estimated from coastal tsunami measurements can be used to reconstruct the realistic open-ocean tsunami spectrum that would be similar to the tsunami spectrum directly evaluated from the DART observations. The main criterion for the effective reconstruction is the consistency of the spectral ratios, i.e., exactly what we see in Figure 14 for the 2004 spectral ratios on and off the coast of Chile. The question, however, is: Do these spectral ratios reflect the properties of the 2004 tsunami signal in the southeastern Pacific or are they more general and specifically related to the spectral properties of the tsunami source? To answer to this question we selected several high-quality records for certain stations in the Indian and Atlantic oceans shown in Figure 1a (see

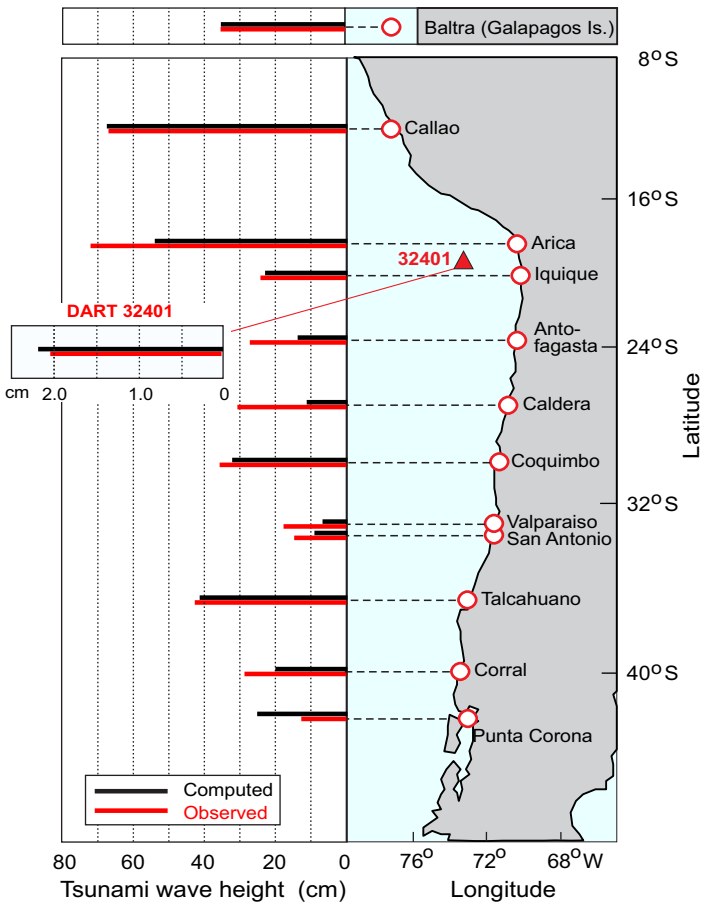

Figure 13. Comparison of computed (black) and observed (red) maximum 2004 tsunami wave heights (adjacent trough-to-crest) at coastal tide gauges (white circles) and DART 32401 (red triangle). Computed and observed maximum wave heights at DART 32401 are shown in the inset.

Candella et al., 2008; Rabinovich & Thomson, 2007; Rabinovich, Candella, et al., 2011) and used the results of their spectral analysis to estimate the respective spectral ratios (Figure 15).

As can be seen from comparison of Figures 14 and 15, the spectral ratios for the Indian Ocean and Atlantic stations are quite similar to those for the southeastern Pacific. The tsunami frequency band, the general triangle shape of the ratios, and even the frequencies of certain particular ratio peaks closely match each other for these three regions. The noticeable differences are only in the absolute values: the stations located closer to the source, i.e., in the Indian Ocean, recorded much stronger tsunami signal and, consequently, have significantly larger $R_j(\omega)$ magnitudes. Except for this factor, the ratios shown in these two figures are alike.

The consistency and similarity of the reconstructed spectral ratios for various regions of the world oceans appears to have a deep physical meaning: these ratios carry the signatures ("birth marks") of the initial tsunami source. Despite numerous random factors distorting the tsunami signal during its global propagation, the ratios keep the principal information about the source, potentially enabling us to reconstruct the origin spectral characteristics of the signal.

The spectral characteristics of the generated waves depends on the dimensions of the tsunami source and the water depth in the source area (h_s). The extension of the source region (L) and the dominant period of the induced tsunami waves (T_t) are roughly related as

$$L \sim T_t \cdot \sqrt{gh_s}. \tag{6}$$

The approximate water depth in the source, $h_s \sim 2500$ m. Thus for $T_t = 40$ min we have $L\,(40) \approx 380$ km.

Fine et al. (2005) based on analysis of altimetric and coastal tide gauge data in the Indian Ocean delineated the 2004 source region and found two main "hot spots": northern slow-slip and southern fast-slip domains; they evaluated that the southern domain had extension of approximately 350 km. Very similar estimates of the southern fast-slip domain were obtained by Stein and Okal (2005), Lay et al. (2005), Ishii et al. (2005), and Fujii and Satake (2007) based on examination of various seismological, GPS and sea level data. All these authors, and many others, indicated that the global impact of the 2004 Sumatra tsunami was associated particularly with this southern "hot source." The consistent character of the 40 min peak in the spectral ratios throughout all oceans (Figures 14 and 15), the worldwide dominance of this period in the 2004 tsunami records (Rabinovich & Thomson, 2007; Rabinovich et al., 2006) and good agreement between $L\,(40)$ and independent estimates of the southern "hot-spot" extension, surely demonstrate that this 40 min period is specifically associated with this fast slip southern source.

The orientation of the source and the directivity of propagating tsunami waves play an important role in spectral composition of tsunamis. In particular, Heidarzadeh and Satake (2013, 2014) demonstrated that the dominant period of the recorded waves significantly depends on the direction of the arriving waves from the source, based on analyses of the 2003 Algerian, 2012 El Salvador and 2012 Philippines tsunamis. In the case of the 2004 Sumatra tsunami, both the Pacific and Atlantic waves were initially emitted from the southern fast-slip domain in the same southwestward direction (Fine et al., 2005); this appears to be the main reason of the similarity of their spectral properties and consistent presence of the 40 min major peak in spectral ratios throughout all ocean basins.

The origin of 23 min peak in the spectral ratios is not so univocal. Rough estimates give $L\,(23) \approx$ 220 km. This value is very close to the cross-source width (200–250 km according to Fine et al. (2005),

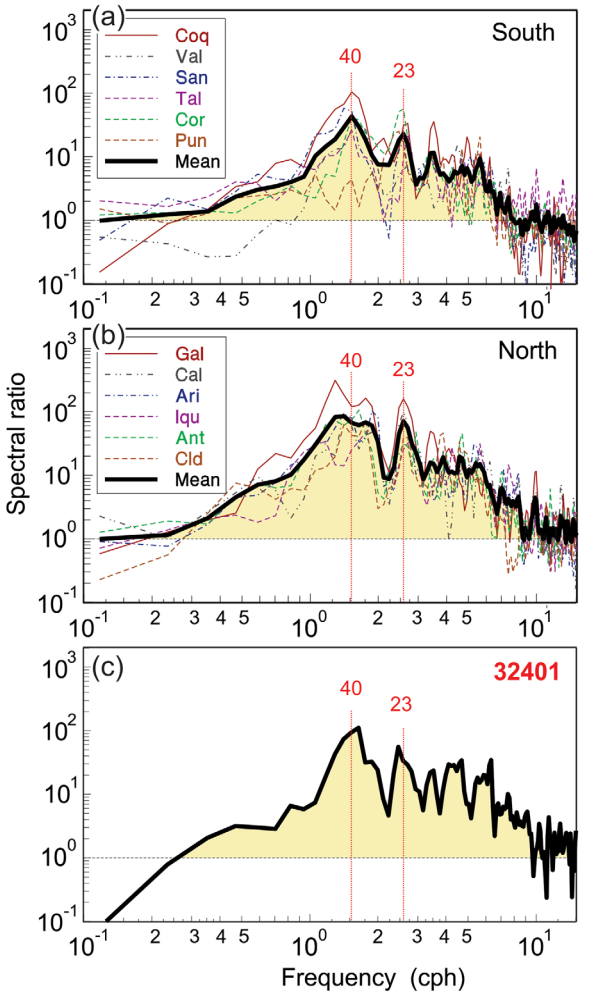

Figure 14. Comparison of observed estimated tsunami-to-background spectral ratios (source functions) for the 2004 Sumatra tsunami along the coast of South America and offshore for: (a) the southern group; (b) the northern group; and (c) DART 32401. Shaded areas denote the mean spectral ratio for each group of stations.

Lay et al. (2005), and Fujii & Satake (2007)). However, it is possible also that this period is related to one of the secondary "hot-spots" of the 2004 tsunami source area identified by Chlieh et al. (2007) based on analysis of the GPS data.

In general, we may assume that while peak values of $\hat{R}(\omega)$ are caused by particular "hot-spots" of the source, the wide tsunami frequency band of 0.25–10 cph (i.e., of periods from 4 h to 6 min) are related to the entire source region of ~1,300 km (cf. Fujii & Satake, 2007; Ishii et al., 2005; Stein & Okal, 2005). The important finding is that these source properties ("birth marks") persist in sea level records for so long time and distance and may be recognized in far remote regions.

This demonstrates a principal possibility of a global tsunami forecast based on the source characteristics only. The successful comparison of the model with the actual observations in the southeastern Pacific validate the high quality and efficiency of the global MOST model. The open ocean measurements at DART 32401 provided the most unambiguous verification of the model, since the record is not contaminated with coastal amplification factors, resonant effects and nonlinearity, i.e., with processes essentially affecting coastal tsunami records. Direct comparison of the computed and observed tsunami waveforms showed very good agreement (Figure 11a).

The MOST model is based on a nondispersive shallow-water approximation (Titov & González, 1997; Titov & Synolakis, 1998); therefore, the wave dispersion may be expected to influence the tsunami waves at such large propagation distances. However, the discrepancy between the simulated and recorded waves is quite small (Figure 11a). Very similar results were obtained by Rabinovich, Woodworth, et al. (2011) for two low-resolution open-ocean stations, DPN and DPS, located in the Drake Passage (see Figure 10 for the station locations). This can be partly explained by the low-frequency nature of the 2004 tsunami due to the enormous rupture area of the 2004 Sumatra source region (~1,300 km long according to Stein & Okal (2005)), which would result in only small dispersion effects. Another reason is that the MOST model exhibits numerical dispersion that reproduces the dispersive equations fairly well (see Burwell et al. (2007) and Shuto (1991) who discussed this problem in details). The application of the MOST model for several recent events in the Pacific Ocean indicated that for low-frequency events the numerical dispersion compares reasonably well to the actual wave dispersion (cf. Tang et al., 2012; Titov, Song et al., 2016; Wei et al., 2008).

The MOST model provided much better agreement between computed and actual 2004 tsunami arrival times than the classical kinematic theory, which is widely used to estimate the Tsunami Travel Time, TTT (see e.g., Satake, 1988; *Woods and Okal*, 1987): the early-arrival discrepancy at DART 32401 was 20 min for the model versus a theoretical 90 min from kinematic estimates. Kinematic theory (based on the ray-tracing algorithm) calculates the "fastest" possible tsunami route from one point to another, which may be followed by very small amplitude waves that may not be detectable, while the wave dynamics computed by MOST global numerical model shows that higher amplitude waves with detectable arrival of the 2004 tsunami waves corresponds to the most "energetically economic" path along the mid-ocean ridge wave-guides (Figure 1), as described by Titov et al. (2005) and Kowalik et al. (2005, 2007).

There are several potential factors that can cause 20 min discrepancy between numerically simulated and observed arrivals of the 2004 tsunami at DART 32401. Some factors that have been discussed in the literature include wave dispersion, the elasticity of the Earth crust and compressibility of the water (Allgeyer and Cummins, 2014; Watada et al., 2014); other factors may include insufficient bathymetry resolution, influence of bottom friction, Earth rotation and possibly more.

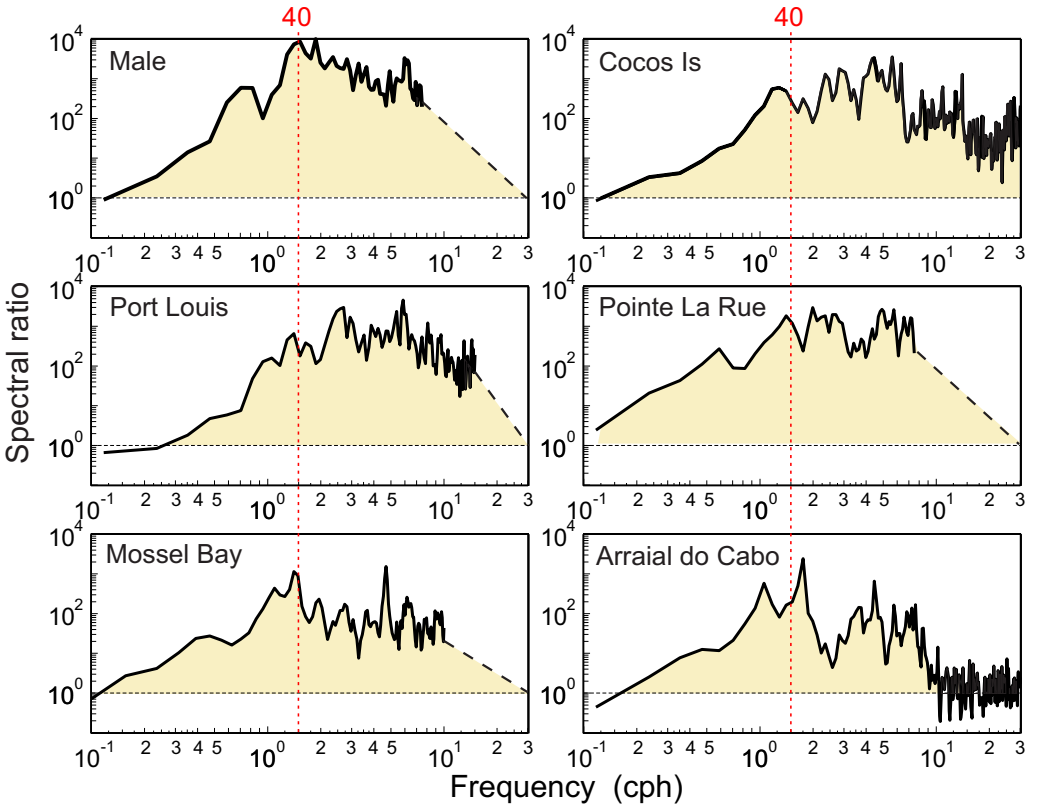

Figure 15. Estimated tsunami-to-background spectral ratios (source functions) for the 2004 Sumatra tsunami for stations located in the Indian and Atlantic oceans. Shaded areas denote the tsunami response associated with the arriving waves; i.e., the amplification of the spectra due to the tsunami waves relative to the background spectra.

8. Conclusions

The 2004 Sumatra tsunami was an unprecedented natural disaster of global affect that attracted great political, humanitarian, public, and scientific attention. The main focus of our study is on the southeastern Pacific Ocean, the region located in 16,000–18,000 km from the source area. The interest to this region is highly stimulated by the fact that this is the convergence zone of circumferentially propagating Atlantic ("westward") and Pacific ("eastward") tsunami waves. The investigation presented here on the far-field behavior of the 2004 tsunami waves relies entirely on the data from one well-placed Chilean DART system 32401 and tide gauges located along the Pacific coast of South America. The study focused on examination of the tsunami wave field and on determining whether (1) the distal records of the 2004 tsunami contained information about the characteristics of the source that could first be distinguished in each record, and (2) numerical simulations based on the seismic source analysis and regional tsunami measurements could accurately reproduce these characteristics in the far-field.

Based on comparative spectral analysis of tsunami and background signals embedded in coastal tide gauges, the influence of topography was successfully suppressed such that reconstructed "spectral ratios" were found to be in agreement with the open-ocean ratio at DART 32401, and with the spectral ratios estimated from coastal records in the Indian and Atlantic oceans. These similarities were striking, especially considering that the spatial scope of evaluation included different oceanic regions and regimes. Such finding is more than mere coincidence and implies that this characteristic reflects the actual spectral parameters of the 2004 tsunami source. Tsunami records, therefore, even from stations located tens of thousands of km away from the source carry source signatures, or "birth marks" that can be efficiently extracted from recorded time series in both the deep ocean and along the shallow coast. Specific analyses of tsunami/background spectral ratios in the southeastern Pacific, showed that the 2004 tsunami waves occupied the

frequency band of 0.25–10 cph (periods from 4 h to 6 min), and that the spectral ratios of this tsunami have a particular consistent triangle shape with two prominent ratio peaks at periods 40 and 23 min.

The period of 40 min was found to be related to the southern fast-slip domain of the 2004 source, more specifically to the "hot spot" within this domain that had extension of approximately 350 km (cf. Fine et al., 2005), in good agreement with roughly estimated expected dimension of the 40 min source, $L\,(40) \approx$ 380 km. What is important, according to numerous studies of the 2004 event (cf. Chlieh et al., 2007; Fine et al., 2005; Fujii & Satake, 2007; Ishii et al., 2005; Stein & Okal, 2005), the "southern source region" was responsible for the global impact of the 2004 Sumatra tsunami and dominant waves that propagated throughout the world oceans and caused most of catastrophic destructions. It is natural that the particular period associated with this "hot spot" prevailed in the far-field records.

The origin of 23 min peak with the estimated $L\,(23) \approx 220$ km is probably related to the cross-source width (200–250 km) or to one of the secondary "hot-spots" of the 2004 source area identified by Chlieh et al. (2007) based on analysis of the GPS data. The general very broad frequency band of the 2004 Sumatra tsunami waves of 0.25–10 cph (periods from 4 h to 6 min) appears to be associated with the entire complicated source region of ~1,200 to 1,300 km (cf. Fujii & Satake, 2007; Stein & Okal, 2005). The important finding is that these source properties ("birth marks") persist in sea level records for such long time and distance and may be recognized in far remote regions.

Use of source parameters alone for model simulated tsunami forecasting is closely related to the concept of a tsunami source "birth mark." The long duration of the global tsunami signal despite numerous factors that scattered, distorted and refocused waves demonstrate the principal possibility of a global tsunami numerical forecast based solely on source characteristics. The information from DART 32401 offshore of northern Chile was especially valuable for verification of the global model use and validation of results. The MOST model numerically simulated maximum tsunami wave amplitude of 2.25 cm at the deep-ocean site provided a close approximation of the measured height (2.05 cm); a difference <9%. The numerically computed tsunami travel time of 25 h 35 min from the Indian Ocean source to DART 32401 was only 20 min earlier than the actual travel time of 25 h 55 min, a favorable result when compared with the travel time of ~24 h 25 min estimated from classical kinematic theory. In addition, MOST numerical simulations consistently reproduced the wave height changes noted along the coast of South America (Figure 13) including local amplification of the tsunami in the southern region (42 cm at Talcahuano), attenuation of the waves in the central region (between San Antonio and Iquique) and maximum wave heights at the northern stations of Arica (72 cm), Callao (67 cm), and on island station Baltra, Galapagos (35 cm).

Identification of tsunami source "birth marks" coupled with validation of numerical modeling at considerably distant deep-ocean and coastal impact sites offers exciting future possibilities.

Acknowledgments
The authors gratefully acknowledge the Servicio Hidrográfico y Oceanográfico de la Armada de Chile (SHOA) for generously providing coastal tide gauge and deep-ocean DART 32401 data. All observation and digital bathymetry data used in the publication can be obtained from repositories of National Data Buoy Center (http://www.ndbc.noaa.gov/dart.shtml), National Center for Environmental Prediction (https://www.ncei.noaa.gov/access) or by request from authors. We would like to thank Drs. Richard Thomson and Isaac Fine (Institute of Ocean Sciences, Sidney, BC, Canada), Prof. Kenji Satake (University of Tokyo, Japan) and an anonymous reviewer for their very helpful comments and suggestions. For A.B.R. this study was partly supported by NOAA project WE-133R-15-SE-1608 and RSF grant 14–50-00095. This is NOAA Pacific Marine Environmental Laboratory contribution number 4620.

References

Allgeyer, S., & Cummins, P. (2014). Numerical tsunami simulation including elastic loading and seawater density stratification. *Geophysical Research Letters*, *41*, 2368–2375. https://doi.org/10.1002/2014GLO59348

Aucan, J., & Ardhuin, F. (2013). Infragravity waves in the deep ocean: An upward revision. *Geophysical Research Letters*, *40*, 3435–3439. https://doi.org/10.1002/grl.50321

Bernard, E., & Titov, V. V. (2015). Evolution of tsunami warning systems and products. *Philosophical Transactions of the Royal Society A*, *373*(2053), 20140371. https://doi.org/10.1098/rsta.2014.0371

Bernard, E. N., González, F. I., Meinig, C., & Milburn, H. B. (2001). Early detection and real-time reporting of deep-ocean tsunamis. In *Proceedings of International Tsunami Symposium* (pp. 97–108), Seattle, WA.

Burwell, D., Tolkova, E., & Chawla, A. (2007). Diffusion and dispersion characterization of a numerical tsunami model. *Ocean Modelling*, *19*(1–2), 10–30.

Candella, R. N., Rabinovich, A. B., & Thomson, R. E. (2008). The 2004 Sumatra tsunami as recorded on the Atlantic coast of South America. *Advances in Geoscience*, *14* (1), 117–128.

Chlieh, M., Avouac, J., Hjorleifsdottir, P. V., Song, T.-R., Ji, A., Sieh, C., . . . Galetzka, J. (2007). Coseismic slip and afterslip of the great (Mw 9.15) Sumatra-Andaman earthquake of 2004. *Bulletin of the Seismological Society of America*, *97*(1A), S152–S173.

Fine, I. V., Rabinovich, A. B., & Thomson, R. E. (2005). The dual source region for the 2004 Sumatra tsunami. *Geophysical Research Letters*, *32*, L16602. https://doi.org/10.1029/2005GL023521

Foreman, M. G. G. (1977/2004), Manual for tidal heights. Analysis and prediction (Pacific Marine Science Rep. 77-10, 58 pp.). Sidney, BC: Institute of Ocean Sciences. Retrieved from http://www-sci.pac.dfo-mpo.gc.ca/osap/publ/online/currents2004.pdf

Fujii, Y., & Satake, K. (2007). Tsunami source of the 2004 Sumatra-Andaman earthquake inferred from tide gauge and satellite data. *Bulletin of the Seismological Society of America*, *97*, 192–207.

Geist, E. L., Titov, V. V., & Synolakis, C. E. (2006). Tsunami: Wave of change. *Scientific American*, *294*(1), 56–63.

González, F. I., Bernard, E. N., Meinig, C., Eblé, M. C., Mofjeld, H. O., & Stalin, S. (2005). The NTHMP tsunameter network. *Natural Hazards*, *35*(1), 25–39.

Heidarzadeh, M., & Satake, K. (2013). The 21 May 2003 tsunami in the Western Mediterranean Sea: Statistical and wavelet analyses. *Pure and Applied Geophysics*, *170*(9–10), 1449–1462. https://doi.org/10.1007/s00024-012-0509-1

Heidarzadeh, M., & Satake, K. (2014). The El Salvador and Philippines tsunamis of August 2012: Insights from sea level data analysis and numerical modeling. *Pure and Applied Geophysics*, *171*(12), 3437–3455. https://doi.org/10.1007/s00024-014-0790-2

Ishii, M., Shearer, P. M., Houston, H., & Vidale, J. E. (2005). Extent, duration and speed of the 2004 Sumatra-Andaman earthquake imaged by the Hi-Net array. *Nature*, *435*, 933–936.

Kânoğlu, U., Titov, V. V., Bernard, E., & Synolakis, C. (2015). Tsunamis: Bridging science, engineering and society. *Philosophical Transactions of the Royal Society A*, *373*, 20140369. https://doi.org/10.1098/rsta.2014.0369

Kowalik, Z., Knight, W., Logan, T., & Whitmore, P. (2005). Numerical modeling of the global tsunami: Indonesian tsunami of 26 December 2004. *Sci. Tsunami Hazards*, *23*(1), 40–56.

Kowalik, Z., Knight, W., Logan, T., & Whitmore, P. (2007). The tsunami of 26 December 2004: Numerical modeling and energy considerations. *Pure and Applied Geophysics*, *164*, 379–393.

Kulikov, E. A., Rabinovich, A. B., Spirin, A. I., Poole, S. L., & Soloviev, S. L. (1983). Measurements of tsunamis in the open ocean. *Marine Geodesy*, *6*, 311–329.

Lay, T., Kanamori, H., Ammon, C. J., Nettles, M., Ward, S. N., Aster, R. C., . . . Sipkin, S. (2005). The Great Sumatra-Andaman earthquake of 26 December 2004. *Science*, *308*, 1127–1133.

Merrifield, M. A., Firing, Y. L., Aarup, T., Agricole, W., Brundrit, G., Chang-Seng, D., . . . Turetsky, N. (2005). Tide gage observations of the Indian Ocean tsunami, December 26, 2004. *Geophysical Research Letters*, *32*, L09603. https://doi.org/10.1029/2005GL022610

Mofjeld, H. O. (2009). Tsunami measurements. In A. Robinson & E. Bernard (Eds.), *The sea, Vol.15, Tsunamis* (pp. 201–235). Cambridge, MA: Harvard University Press.

Mungov, G., Eblé, M., & Bouchard, R. (2013). DART® tsunameter retrospective and real-time data: A reflection on 10 years of processing in support of tsunami research and operations. *Pure and Applied Geophysics*, *170*(9-10), 1369–1384. https://doi.org/10.1007/s00024-012-0477-5

Munk, W. H., Zetler, B., & Groves, G. W. (1965). Tidal cusps. *Geophysical Journal of Royal Astronomical Society*, *10*(2), 211–219. https://doi.org/10.1111/j.1365-246X.1965.tb03062.x

Pugh, D. T. (1987). *Tides, surges and mean sea-level* (472 pp.). Chichester, UK: John Wiley.

Rabinovich, A. B. (1997). Spectral analysis of tsunami waves: Separation of source and topography effects. *Journal of Geophysical Research*, *102* (C6), 12,663–12,676.

Rabinovich, A. B. (2009). Seiches and harbor oscillations. In Y. C. Kim (Ed.) *Handbook of coastal and ocean engineering* (pp. 193–236). Singapore: World Scientific.

Rabinovich, A. B., Candella, R., & Thomson, R. E. (2011). Energy decay of the 2004 Sumatra tsunami in the world ocean. *Pure and Applied Geophysics*, *168*(11), 1919–1950. https://doi.org/10.1007/s00024-01-0279-1

Rabinovich, A. B., & Eblé, M. (2015). Deep-ocean measurements of tsunami waves. *Pure and Applied Geophysics*, *172*(12), 3281–3312. https://doi.org/10.1007/s00024-015-1058-1

Rabinovich, A. B., Geist, E. L., Fritz, H. M., & Borrero, J. C. (2015). Introduction to "Tsunami Science: Ten Years after the 2004 Indian Ocean Tsunami. Volume I. *Pure and Applied Geophysics*, *172*(3–4), 615–619. https://doi.org/10.1007/s00024-015-1038-5

Rabinovich, A. B., Stroker, K., Thomson, R. E., & Davis, E. (2011). DARTs and CORK: High-resolution observations of the 2004 Sumatra tsunami in the abyssal northeast Pacific. *Geophysical Research Letters 38*, L08502. https://doi.org/10.1029/2011GL047063

Rabinovich, A. B., & Thomson, R. E. (2007). The 26 December 2004 Sumatra tsunami: Analysis of tide gauge data from the World Ocean Part 1. Indian Ocean and South Africa. *Pure and Applied Geophysics*, *164*(2/3), 261–308.

Rabinovich, A. B., Thomson, R. E., & Stephenson, F. E. (2006). The Sumatra tsunami of 26 December 2004 as observed in the North Pacific and North Atlantic Oceans. *Surveys in Geophysics*, *27*, 647–677.

Rabinovich, A. B., Woodworth, P. L., & Titov, V. V. (2011). Deep-sea observations and modeling of the 2004 Sumatra tsunami in Drake Passage. *Geophysical Research Letters*, *38*, L16604. https://doi.org/10.1029/2011GL048305

Satake, K. (1988). Effects of bathymetry on tsunami propagation: Application of ray tracing to tsunamis. *Pure and Applied Geophysics*, *126*(1), 27–36.

Satake, K., & Kanamori, H. (1991). Use of tsunami waveforms for earthquake source study. *Natural Hazards*, *4*, 193–208.

Satake, K., Okal, E. A., & Borrero, J. C. (2007). Tsunami and its hazard in the Indian and Pacific oceans: Introduction. *Pure and Applied Geophysics*, *164*, 249–259. https://doi.org/10.1007/s00024-006-0172-5

Shevchenko, G., Ivelskaya, T., Loskutov, A., & Shishkin, A. (2013). The 2009 Samoan and 2010 Chilean tsunamis recorded on the Pacific coast of Russia. *Pure and Applied Geophysics*, *170*(9–10), 1511–1527. https://doi.org/10.1007/s00024-012-0562-9

Shuto, N. (1991). Numerical simulation of tsunamis–Its present and near future. *Natural Hazards*, *4*, 171–191.

Smith, W., Scharroo, R., Titov, V. V., Arcas, D., & Arbic, B. K. (2005). Satellite altimeters measure tsunami. *Oceanography*, *18*(2), 10–12.

Stein, S., & Okal, E. A. (2005). Speed and size of the Sumatra earthquake. *Nature*, *434*, 581–582.

Tang, L., Titov, V. V., Bernard, E. N., Wei, Y., Chamberlin, C. D., Newman, J. C., . . . Gica, E. (2012). Direct energy estimation of the 2011 Japan tsunami using deep-ocean pressure measurements. *Journal of Geophysical Research*, *117*, C08008. https://doi.org/10.1029/2011JC007635

Thomson, R. E., & Emery, W. J. (2014). *Data analysis methods in physical oceanology* (3rd ed., 716 pp.). New York: Elsevier.

Thomson, R. E., Rabinovich, A. B., & Krassovski, M. V. (2007). Double jeopardy: Concurrent arrival of the 2004 Sumatra tsunami and storm-generated waves on the Atlantic coast of the United States and Canada. *Geophysical Research Letters*, *34*, L15607. https://doi.org/10.1029/2007GL030685

Titov, V., Song, T., Tang, L., Bernard, E. N., Bar-Severt, Y., & Wei, Y. (2016). Consistent estimates of tsunami energy show promise for improved early warning. *Pure and Applied Geophysics*, *173*(12), 3863–3880. https://doi.org/10.1007/s00024-016-1312-1

Titov, V. V. (2009). Tsunami forecasting. In A. Robinson & E. Bernard (Eds.) *The sea, Vol.15, Tsunamis* (pp. 371–400). Cambridge, MA: Harvard University Press.

Titov, V. V., & González, F. I. (1997). Implementation and testing of the Method of Splitting Tsunami (MOST) model (NOAA Technical Memorandum ERL PMEL-112). Seattle, WA: Pacific Marine Environmental Laboratory.

Titov, V. V., Kânoğlu, U., & Synolakis, C. (2016). Development of MOST for real-time tsunami forecasting. *Journal of Waterway, Port, Coastal, and Ocean Engineering*. https://doi.org/10.1061/(ASCE) WW.1943–5460.0000357

Titov, V. V., Rabinovich, A. B., Mofjeld, H., Thomson, R. E., & González, F. I. (2005). The global reach of the 26 December 2004 Sumatra tsunami. *Science*, *309*, 2045–2048.

Titov, V. V., & Synolakis, C. S. (1998). Numerical modeling of tidal wave runup. *Journal of Waterway, Port, Coastal, and Ocean Engineering*, *124*(4), 157–171.

Vich, M., & Monserrat, S. (2009). The source spectrum for the Algerian tsunami of 21 May 2003 estimated from coastal tide gauge data. *Geophysical Research Letters*, *36*, L20610. https://doi.org/10.1029/2009GL039970

Watada, S., Kusumoto, S., & Satake, K. (2014). Traveltime delay and initial phase reversal of distant tsunamis coupled with the self-gravitating elastic Earth. *Journal of Geophysical Research: Solid Earth*, *119*, 4287–4310. https://doi.org/10.1002/2013JB010841

Webb, S. C., Zhang, X., & Crawford, W. (1991). Infragravity waves in the deep ocean. *Journal of Geophysical Research*, *96*(C2), 141–144.

Wei, Y., Bernard, E. N., Tang, L., Weiss, R., Titov, V. V., Moore, C. . . . Kânoğlu, U. (2008). Real-time experimental forecast of the Peruvian tsunami of August 2007 for U.S. coastlines. *Geophysical Research Letters*, *35*, L04609. https://doi.org/10.1029/2007GL032250

Woods, M. T., & Okal, E. A. (1987). Effect of variable bathymetry on the amplitude of teleseismic tsunamis: A ray-tracing experiment. *Geophysical Research Letters*, *14*(7), 765–768. https://doi.org/10.1029/GL014i007p00765

Woodworth, P. L., Blackman, D. L., Foden, P., Holgate, S., Horsburgh, K., Knight, P. L., . . . Bradshaw, D. E. (2005). Evidence for the Indonesian tsunami in British tidal records. *Weather*, *60* (9), 263–267.

Zaytsev, O., Rabinovich, A. B., & Thomson, R. E. (2016). A comparative analysis of coastal and open-ocean records of the great Chilean tsunamis of 2010, 2014 and 2015 off the coast of Mexico. *Pure and Applied Geophysics*, *173*(12), 4139–4178. https://doi.org/10.1007/s00024-016-1407-8

Zaytsev, O., Rabinovich, A. B., & Thomson, R. E. (2017). The 2011 Tohoku tsunami on the coast of Mexico: A case study. *Pure and Applied Geophysics*, *174*(8), 2961–2986. https://doi.org/10.1007/s00024-017-1593-z